A Cytoskeletal Vortex Drives Phage Nucleus Rotation During Jumbo Phage Replication in *E. coli*

Authors:

Erica A. Birkholz[1], Thomas G. Laughlin[1], Emily Armbruster[1], Sergey Suslov[1], Jina Lee[1], Johannes Wittmann[2], Kevin D. Corbett[3,4], Elizabeth Villa[1,5]‡, Joe Pogliano[1]‡†

Affiliations:

[1]Division of Biological Sciences, University of California, San Diego, La Jolla, CA, 92093, USA

[2]Leibniz Institute DSMZ–German Collection of Microorganisms and Cell Cultures, Braunschweig, 38124, Germany

[3]Department of Cellular and Molecular Medicine, University of California, San Diego, La Jolla, CA, 92093, USA

[4]Department of Chemistry and Biochemistry, University of California, San Diego, La Jolla, CA, 92093, USA

[5]Howard Hughes Medical Institute, University of California, San Diego, La Jolla, CA, 92093, USA

‡ Correspondence: evilla@ucsd.edu, jpogliano@ucsd.edu

† Lead Contact

Summary

Nucleus-forming jumbo phages establish an intricate subcellular organization, enclosing phage genomes within a proteinaceous shell called the phage nucleus. During infection in *Pseudomonas*, some jumbo phages assemble a bipolar spindle of tubulin-like PhuZ filaments that positions the phage nucleus at midcell and drives its intracellular rotation. This facilitates the distribution of capsids on its surface for genome packaging. Here we show that the *E. coli* jumbo phage Goslar assembles a phage nucleus surrounded by an array of PhuZ filaments resembling a vortex instead of a bipolar spindle. Expression of a mutant PhuZ protein strongly reduces Goslar phage nucleus rotation, demonstrating that the PhuZ cytoskeletal vortex is necessary for rotating the phage nucleus. While vortex-like cytoskeletal arrays are important in eukaryotes for cytoplasmic streaming and nucleus alignment, this work identifies a coherent assembly of filaments into a vortex-like structure driving intracellular rotation within the prokaryotic cytoplasm.

Introduction

Subcellular organization is essential for all domains of life, including viruses (Chaikeeratisak et al., 2021a; Charman and Weitzman, 2020). We recently identified a nucleus-like structure (Chaikeeratisak et al., 2017b) formed by *Pseudomonas chlororaphis* jumbo phage 201φ2-1 (Thomas et al., 2012, 2010, 2008), which was subsequently shown to be conserved (Chaikeeratisak et al., 2017a; Danilova et al., 2020) in related phages ΦKZ (Krylov et al., 2021; Lecoutere et al., 2009; Mesyanzhinov et al., 2002; Weintraub et al., 2019), and ΦPA3 (Monson et al., 2011). Analogous to a eukaryotic nucleus, the phage nucleus imparts strict separation of transcription from translation by enclosing phage DNA within a proteinaceous shell that excludes ribosomes (Chaikeeratisak et al., 2017b). This separation requires the export of mRNA to the cytoplasm for translation and the selective import of proteins required for transcription, DNA replication, and DNA repair. The phage nucleus protects the phage DNA by excluding restriction enzymes and DNA-targeting CRISPR-Cas in both *Pseudomonas* and *Serratia* jumbo phages (Malone et al., 2020; Mendoza et al., 2020; Nguyen et al., 2021). The phage nuclear shell is primarily composed of a single protein, termed chimallin, which forms a single layer-thick flexible lattice with pores ~2 nm in diameter (Laughlin et al., 2022). The small pore size in the chimallin lattice suggests that the nuclear shell also incorporates minor components with specialized roles in mRNA export and specific protein import (Laughlin et al., 2022). The phage nucleus grows as phage DNA is replicated inside and it is positioned and rotated in the center of the cell by a bipolar spindle composed of filaments of the tubulin-like PhuZ protein (Chaikeeratisak et al., 2017b; Erb et al., 2014; Kraemer et al., 2012). The phage nucleus and spindle are also important for jumbo phage diversification because they contribute to the evolution of new species through Subcellular Genetic Isolation and Virogenesis Incompatibility (Chaikeeratisak et al., 2021b).

Early in the nucleus-forming jumbo phage infection process, the phage nucleus is maneuvered towards the center of the host cell and oscillates in position once it reaches the midcell due to stochastic growth and shrinkage of PhuZ filaments in the bipolar spindle (Chaikeeratisak et al., 2017b; Erb et al., 2014; Kraemer et al., 2012). PhuZ was first identified in phage 201φ2-1, which infects *P. chlororaphis,* and was shown to form a three-stranded polar filament with dynamic (+) and (-) ends, analogous to eukaryotic microtubules (Erb et al., 2014; Kraemer et al., 2012; Zehr et al., 2014). The (-) ends of the spindle are positioned at each cell pole, while the (+) ends point toward the midcell. PhuZ filaments display dynamic instability during which the (+) ends rapidly depolymerize until returning to a growth phase, thereby allowing the spindle to position the phage nucleus in the center of the cell (Chaikeeratisak et al., 2017a, 2017b; Erb et al., 2014; Kraemer et al., 2012). Like the phage nucleus, PhuZ was later shown to be conserved in the *P. aeruginosa* phages ΦKZ and ΦPA3 (Aylett et al., 2013; Chaikeeratisak et al., 2017a).

During the later phases of the nucleus-forming jumbo phage replication cycle, PhuZ filaments exhibit treadmilling when they polymerize at the cell pole at a rate similar to depolymerization at the surface of the nucleus (Chaikeeratisak et al., 2019). Treadmilling filaments apply pushing forces to opposing sides of the phage nucleus, causing it to rotate (Chaikeeratisak et al., 2019, 2017b). Capsids, which assemble on the cell membrane, attach to treadmilling filaments of the PhuZ spindle and are trafficked to the surface of the phage nucleus where they dock for packaging of the genome (Chaikeeratisak et al., 2019). As the PhuZ spindle rotates the phage nucleus, capsids are distributed to different locations on its surface, likely in order to promote efficient DNA packaging. These functions of the PhuZ spindle, including the remarkable capacity for driving

intracellular rotation of the phage nucleus, are conserved in all three *Pseudomonas* jumbo phages described above (Chaikeeratisak et al., 2019, 2017a, 2017b; Kraemer et al., 2012). Studies with dominant negative PhuZ mutants suggest that these functions are not essential, but they are important for the maximum production of virions (Kraemer et al., 2012).

To add to the intricacies of this replication mechanism, these nucleus-forming jumbo phages encode two multi-subunit RNA polymerases, one of which is packaged into the virion and transcribes early genes (Ceyssens et al., 2014; Lecoutere et al., 2009; Sokolova et al., 2020). The non-virion multi-subunit RNA polymerase is expressed during infection and transcribes late genes (Ceyssens et al., 2014; Orekhova et al., 2019; Sokolova et al., 2020; Yakunina et al., 2015). In addition, we recently described the organization of maturing virion particles into phage bouquets (Chaikeeratisak et al., 2022). These nearly spherical structures are formed by viral particles undergoing final assembly with tails pointing inward, resembling a bouquet of flowers. Bouquets are established in the final stages of the nucleus-forming jumbo phage replication cycle when fully packaged capsids move from the surface of the phage nucleus to the regions adjacent to the nucleus. The interior of bouquets largely excludes ribosomes and cytoplasmic GFP (Chaikeeratisak et al., 2022). Eventually, the cell lyses, releasing the progeny phages into the environment.

It is still unknown how widespread this replication pathway may be among jumbo phages; assembly of a phage nucleus has only been observed in the above-mentioned *Pseudomonas* phages and *Serratia* phage PCH45, while the PhuZ cytoskeleton has only been studied in *Pseudomonas*. In order to further understand if phage nucleus formation and positioning, bipolar PhuZ spindle

assembly, intracellular rotation of the phage nucleus, capsid trafficking, and phage bouquets are conserved among more diverse jumbo phage, we sought out a nucleus-forming jumbo phage that infects *Escherichia coli*. Here we characterize the reproduction pathway of phage vB_EcoM_Goslar (Goslar) (Korf et al., 2019). We show that Goslar is a nucleus-forming jumbo phage that assembles a vortex-like cytoskeletal array instead of a bipolar spindle that drives phage nucleus rotation. PhuZ mutations that disrupt vortex assembly also disrupt phage nucleus rotation, linking the cytoskeletal vortex to a remarkable process in the phage replication cycle. Our results show that the nucleus-forming phage infection pathway is likely widespread and diverse strategies have evolved to achieve intracellular rotation of the phage nucleus.

Results

E. coli jumbo phage Goslar forms a phage nucleus

E. coli phage vB_EcoM_Goslar (Goslar) was recently discovered and sequenced (Korf et al., 2019), revealing distantly related homologs of the PhuZ spindle protein and the major phage nucleus shell protein Chimallin (ChmA) (Figures S1A and S1B). We studied the progression of Goslar through the lytic cycle in the *E. coli* K-12 lab strain MG1655 and compared basic infection morphology in the isolation host, APEC 2248 (APEC), to ensure our findings in the lab strain represented the replication pathway in the original host. We found that host chromosomal DNA was largely degraded by 60 minutes post-infection (mpi) as a dense ball of phage DNA accumulated, visible by DIC as well as DAPI staining (Figures S1C-S1E), similar to infection of *Pseudomonas* by nucleus-forming phages (Erb et al., 2014; Kraemer et al., 2012). To determine whether the Goslar DNA ball is surrounded by a proteinaceous shell, we tagged a homolog of 201φ2-1 Chimallin, Goslar gp189, (21.52% amino acid identity with gp105 of 201φ2-1; Figure S1A), with GFP on the N-terminus and expressed it from a plasmid by induction with 0.2 mM IPTG. In uninfected cells, fluorescence from the GFP-ChmA fusion was diffuse (Figure S2A). In infected cells imaged without added dyes, GFP-ChmA formed a distinct halo around the DNA density observed by DIC (Figures 1A and S2C). We occasionally observed GFP puncta within the halo. When visualized with FM4-64 and DAPI added to the imaging pad at 30, 60, and 90 mpi, GFP-ChmA surrounded the DNA (Figure 1D), suggesting that Goslar is a nucleus-forming phage.

We next tested whether Goslar establishes a compartment that is distinct from the cytoplasm and selectively imports proteins. Using fluorescent protein fusions, we found that the Goslar-encoded protein gp193 of unknown function localizes with the Goslar phage nucleus. We co-expressed

GFP-ChmA with gp193-mCherry and found that gp193-mCherry puncta were either clearly inside the GFP-ChmA shell (28%), inside the shell but also associated with it (43%), or colocalized with the surface (29%) (n=100; Figure 1B). Both fusions were diffuse when co-expressed in uninfected cells (Figure S2B). We observed the same association of gp193 with the phage DNA when gp193 was tagged with other fluorescent proteins (GFP, GFPmut1, mEGFP) on either terminus (Figures S2D-S2E). These results demonstrate that in 100% (n=100) of infections, gp193 was associated with the phage nucleus and never elsewhere in the cytoplasm, showing that it is selectively localized with the phage DNA.

The phage nuclei of the *Pseudomonas* jumbo phages exclude ribosomes and metabolic proteins (Chaikeeratisak et al., 2017b) so we examined the localization of the *E. coli* 50S ribosomal protein L20 (RplT) and thymidylate kinase (TMK) fused to GFP, as well as GFP alone. RplT-GFP, TMK-GFPmut1, and GFP were all diffuse in uninfected cells (Figure S2F) and they were largely excluded from the phage nucleus during infection (Figure 1C), demonstrating that the phage nucleus forms a compartment that is distinct from the cell cytoplasm. These data suggest that the Goslar phage nucleus successfully segregates DNA from ribosomes and metabolic enzymes, thereby uncoupling transcription from translation.

In order to examine the ultrastructure and molecular organization of the phage nucleus, we performed cryo-focused ion beam milling coupled with cryo-electron tomography (cryo-FIB-ET) on Goslar-infected APEC cells at late stages of infections (~90 mpi) (Figures 1E and 1F). Despite the distant sequence homology of Chimallin (Figure S1A), the ultrastructure of the Goslar phage nucleus is strikingly similar to phage nuclei observed in the previously characterized *Pseudomonas*

jumbo phages. The perimeter of the Goslar nucleus appears to be composed of a single layer of protein approximately 6 nm thick. In agreement with our fluorescence microscopy results, the Goslar nucleus separates phage DNA from the cytosol and is devoid of host ribosomes (Figures 1E and 1F). Capsids containing various amounts of DNA, based on the density within the capsids, were docked on the surface of the phage nucleus shell, representing various stages of Goslar DNA packaging (Figure 1E).

Goslar forms a vortex-like array of PhuZ filaments

Goslar encodes a divergent homolog (gp201) of the phage cytoskeletal protein PhuZ (26.96% amino acid identity with 201φ2-1 gp59; Figure S1B). To determine whether this divergent homolog forms a bipolar spindle that organizes phage replication similarly to the nucleus-forming *Pseudomonas* jumbo phages, we tagged the N-terminus of Goslar gp201 with GFP and visualized it with fluorescence microscopy *in vivo*. Since the polymerization of tubulins like PhuZ occurs spontaneously above a critical concentration of monomers, we chose a concentration of IPTG (0.2 mM) for induction of GFP-PhuZ that resulted in spontaneous filament formation in less than 0.5% of cells (Figures S3B and S3C), but strongly labeled PhuZ filaments in infected cells (Figures 2A and 2B). During infection by Goslar, GFP-PhuZ was incorporated into filaments that organized into a vortex-like array around the phage nucleus (Figures 2A, 2B, see model in 2D). The percentage of cells containing GFP-PhuZ filaments increased from 19% (n=75) at 30 mpi to 97% (n=114) at 60 mpi (Figure 2C). At 30 mpi, one or two long filaments (yellow) could be observed in some cells (Figure 2A). By 60 mpi, GFP-PhuZ filaments were arranged into a vortex wrapping around the phage nucleus (visualized by DAPI-staining and as a DIC density) and terminating at the membrane with some reaching the cell poles (Figure 2A). This vortex-like cytoskeletal

structure remained assembled at both 90 mpi and 120 mpi (Figure 2B). In some cells, two long filaments flanked the phage nucleus, similar to the bipolar spindle of *Pseudomonas* nucleus-forming jumbo phage. However, in contrast to the *Pseudomonas* phages' PhuZ spindle, in Goslar these longer filaments were always accompanied by smaller PhuZ filaments around the phage nucleus, forming a vortex. When GFP-PhuZ was expressed at lower induction levels, including 20 μM IPTG and 100 μM IPTG, the cytoskeletal vortex was still observed (Figure S3A). Even without any IPTG present, GFP signal from the fusion protein was most concentrated around the periphery of the phage DNA visualized by DIC, although the signal was very low. These results suggest that GFP-PhuZ filaments wrap around the phage nucleus and create a vortex-like cytoskeletal structure (Figure 2D) and that the vortex is not due to an artifact of overexpression.

To better visualize the spatial relationship between the PhuZ vortex and the phage nucleus, we simultaneously visualized the Goslar Chimallin shell and PhuZ filaments by expressing GFP-ChmA and mCherry-PhuZ from the same plasmid with 0.2 mM IPTG. At 90 mpi, the mCherry-PhuZ filaments (magenta) wrapped around the GFP-ChmA (yellow) and protruded towards the membrane in all directions (Figure 3A). To determine whether the choice of fluorescent protein fusion affected the co-localization, we also imaged mCherry-ChmA (magenta) with GFP-PhuZ (yellow) and found a similar organization (Figure 3B). In time course experiments, we found that at 30 mpi the shell of the phage nucleus had grown to the point that it was clearly distinguishable as a compartment containing DAPI-stained DNA and it was typically accompanied by small PhuZ filaments (Figure 3C). By 60 mpi and beyond, the filaments co-localized with the phage nucleus surface and assembled a cytoskeletal vortex. This contrasts with the bipolar spindle assembled by nucleus-forming *Pseudomonas* phages, where filaments emanate from each pole of the cell and

extend toward the phage nucleus at the cell center, providing the pushing forces necessary for both positioning and rotation (see model in Figure 4D) (Chaikeeratisak et al., 2019, 2017b; Erb et al., 2014; Kraemer et al., 2012). Thus, the vortex-like organization of PhuZ filaments during Goslar infections represents a type of cytoskeletal structure not previously found in prokaryotes.

The Goslar nucleus is not positioned at midcell

The bipolar PhuZ spindle of *Pseudomonas* jumbo phages uses dynamic instability to center the phage nucleus. However, we measured the position of the Goslar phage nucleus and found that, unlike nucleus-forming *Pseudomonas* phages, the Goslar nucleus was not specifically positioned at any one location along the cell length, in neither MG1655 nor APEC (Figures 3D and 3F). In fact, the likelihood of finding a Goslar nucleus near the midcell was not significantly greater than finding it elsewhere in the cell. The Goslar nucleus grew in size over time as DNA was replicated inside, ultimately reaching an average 2D area of ~4 μm^2 (Figures 3E and 3G). These data suggest that the Goslar-encoded distantly related PhuZ protein does not position the growing phage nucleus at midcell.

Goslar nucleus rotation is dependent on vortex orientation and PhuZ function

Midway through the infection cycle, the phage nucleus of *Pseudomonas* phages 201φ2-1, ΦKZ, and ΦPA3 begins to rotate due to the opposing forces of the PhuZ spindle (see model in Figure 4D) (Chaikeeratisak et al., 2019, 2017b). Rotation is coupled to the delivery of capsids to the surface of the phage nucleus and disrupting PhuZ filament dynamics results in the production of 50% fewer phage virions (Kraemer et al., 2012). We collected time-lapse images of the GFP-tagged Chimallin shell every 4 seconds and found that the Goslar phage nucleus rotates (Figure

4A, see Video 1). We also used DIC imaging to visualize and quantify nucleus rotation without the potential interference of any fluorescent stains or protein fusions (Figure 4B, see Video 2). The direction of phage nucleus rotation occurred along any plane relative to the long axis of the cell and sometimes appeared to reverse direction. We measured the rate of rotation using the distance a point traveled along the perimeter of the phage nuclei, when that point appeared to be traveling along the focal plane. Reporting this rate in linear velocity allows for comparison to the rate of PhuZ polymerization and nucleus rotation reported for the *Pseudomonas* phages *(Chaikeeratisak et al., 2019)*. We found an average linear velocity of 50 ± 13 nm/s (measured at the nucleus periphery; n=20; Figure 4C). This average rate of movement is nearly identical to the rates of nucleus rotation and PhuZ filament growth for the nucleus-forming *Pseudomonas* phages (Chaikeeratisak et al., 2019). Rotation is therefore a conserved aspect of the nucleus-forming jumbo phage replication cycle.

We hypothesized a model of nucleus rotation for Goslar in which the PhuZ cytoskeletal vortex provides pushing forces tangentially to the surface of the phage nucleus (Figure 4D). This model predicts that the direction of nucleus rotation should be correlated with the orientation of filaments within the vortex, and that mutations that disrupt PhuZ filament dynamics by inactivating GTP hydrolysis will reduce the rate of rotation. To test the first prediction, we examined the direction of nucleus rotation relative to the orientation of the filaments. Nucleus rotation was observed using DIC time-lapse at 60 mpi and 90 mpi in cells induced with 0.2 mM IPTG to express GFP-PhuZ, and the PhuZ cytoskeleton was observed at a single time point just prior to the time-lapse. As shown in Figure 4E, the nucleus in the top panels rotated counterclockwise while the nucleus in the bottom panels rotated clockwise, and in both cases the cytoskeletal filaments were arranged in

such a way that filament elongation would drive rotation of the phage nucleus in the corresponding direction. These results are consistent with a model in which the vortex of filaments drives rotation of the nucleus by pushing against the cell membrane (Figure 4D).

In order to further test this model, we mutated a conserved PhuZ aspartic acid residue, D202, to an alanine to disrupt the putative site of GTP hydrolysis. Expression of this mutant protein PhuZ(D202A) in uninfected cells yielded filaments in 56% of cells during induction with only 0.02 mM IPTG (Figures S4A and S4B), whereas filaments are only observed for wild-type PhuZ above 0.3 mM IPTG (Figures S3B and S3C). The ability of the mutant to assemble visible filaments when expressed at a much lower level compared to wild-type PhuZ suggests that the D202A mutation disrupts PhuZ polymer dynamics by inhibiting GTP hydrolysis. Based on our prior studies creating similar mutations in phage and plasmid-encoded tubulins (Erb et al., 2014; Kraemer et al., 2012; Larsen et al., 2007), we expected GFP-PhuZ(D202A) to behave as a dominant-negative mutant that could co-assemble with wild-type PhuZ to form inactive polymers. During Goslar infection in the presence of GFP-PhuZ(D202A) induced with 0.2 mM IPTG, the mutant protein failed to form a vortex (Figure 5A), yet phage nuclei positioning and growth appeared to be unaffected compared to GFP-PhuZ (Figures S5A-S5E). However, in time-lapse microscopy, the intracellular rotation of phage nuclei was greatly reduced (Figure 5B, see Videos 3 and 4). We measured the rates of rotation in cells expressing GFP-tagged PhuZ for comparison to the previous measurements in cells with no fusion proteins, to ensure there are no drastic effects on rotation due to GFP-tagging. In the presence of wild-type GFP-PhuZ, 92% (n=265; Figure 5C) of nuclei rotated visibly by DIC with an average linear velocity of 44 ± 9 nm/s (n=20; Figures 5D and S4C-S4D, black dotted lines). This behavior was similar to rotation in the absence of any

fusion proteins (97% rotated, n=105, Figure 5C; 50 ± 13 nm/s, n=20, Figure 5D; Figure S4C, red dotted line). However, the expression of GFP-PhuZ(D202A) during Goslar infection resulted in only 29% (n=101; Figure 5C) of nuclei rotating. Those 29% had an average linear velocity of 18 ± 9 nm/s (n=23; Figure 5D; Figure S4D, magenta dotted line), significantly slower than both wild-type conditions (*unpaired t-test,* 95% CI). The disruption of function by expression of PhuZ(D202A) is likely not complete in some cells due to the presence of wild-type PhuZ expressed by the phage. These results are consistent with a model in which the PhuZ vortex is required for Goslar nucleus rotation.

Goslar forms bouquets of mature virions

As the PhuZ cytoskeleton of nucleus-forming *Pseudomonas* phages rotates the phage nucleus, it simultaneously delivers capsids to the surface of the nucleus for DNA packaging (Chaikeeratisak et al., 2019). Once filled with DNA, maturing phage particles assemble structures we recently termed "phage bouquets" (Chaikeeratisak et al., 2022). We therefore investigated whether Goslar also forms phage bouquets late in the infection cycle by tagging the putative Goslar capsid protein, gp41, with GFP at its C-terminus. At 90 mpi, several stages of capsid organization were visible. In some cells, capsid-GFP was found around the nucleus, where the capsids were likely docked and in the process of packaging phage DNA (Figures 6A and S6A, left panels). We also observed the formation of spherical structures of capsid protein adjacent to the phage nucleus, putative phage bouquets, with capsids also appearing within the centers of the bouquets (Figures 6A and S6A, middle panels, white arrowheads). Since *Pseudomonas* phage bouquets have not been shown to have capsids localized to the interior of the bouquet (Chaikeeratisak et al., 2022), this could be a

newly observed type of bouquet organization. Finally, in very swollen cells, capsids accumulated in the cytoplasm without any obvious organization (Figures 6A and S6A, right panels).

To demonstrate whether capsids within these spherical structures are filled with DNA, we stained Goslar infections with 10 μg/ml DAPI at 90 mpi, 30 minutes before imaging, because the addition of DAPI prior to infection halted phage replication in MG1655 (Figure 6B). We observed a spherical pattern of faint DAPI staining, similar to the capsid-GFP localization and consistent with DNA-filled capsids arranged in a bouquet (white arrows). Curiously, no DAPI staining was visible in the interior of the bouquets, despite observing capsid-GFP localized in this region. To visualize bouquets formed in the presence of DAPI, we used the APEC strain which could be grown in 200 ng/ml DAPI without inhibiting phage replication. The presence of DAPI throughout the entire infection allowed capsids to be stained prior to organizing into the bouquets. This resulted in very bright staining of spherically shaped DAPI-stained phage bouquets that also contained DAPI staining within the interior of the bouquet (Figure 6C), in agreement with the observed capsid protein localization (Figure 6A). Cells with a single phage nucleus typically contained one or two bouquets that could be found on either side of the phage nucleus (Figure 6C). The DAPI-staining of Figure 6C left panels is presented as a 3D reconstruction in Videos 5 and 6. An example of a cell with two phage nuclei and three phage bouquets is shown in Figure 6C with more examples of bouquets in Figure S6B. The length and width of 105 bouquets at a median focal plane is displayed as a scatter plot in Figure S6C. Phage bouquets could become larger than the nucleus, reaching over 2 μm in width and over 5 μm in length, with a median maximum dimension of 1.5 ± 0.75 μm (Figure S6D).

These observations suggest that Goslar capsids are organized into spherically shaped formations with the tails packed together as observed in the *Pseudomonas* phages (Chaikeeratisak et al., 2022), that deform as they enlarge, filling the cell with capsids in the center, which was not previously observed for the *Pseudomonas* phages (Figure 6D). To further investigate this model and better understand the stages of capsid localization, we simultaneously visualized capsid-GFP and DAPI staining at various times post infection (30, 40, 50, 70, and 90 minutes) (Figure 6E). We were not able to express capsid-GFP in APEC so we colocalized capsid-GFP with DAPI in MG1655. At early time points (30 mpi), the capsid fusion was found near the membrane and in the cytosol and lacked DAPI staining or it was concentrated around the nucleus (Figure 6E). By 40 mpi, small spherical bouquets stained with DAPI were found next to the DAPI-filled nucleus (Figure 6E, white arrow). Between 40 and 50 mpi, the small bouquets expanded and acquired internal capsids but only the exterior ring of capsids was stained with DAPI in MG1655 as discussed above. This time course resembles the trafficking of capsids from the membrane to the nuclear shell as described for the nucleus-forming *Pseudomonas* phages (Chaikeeratisak et al., 2019) and the assembly of bouquets of DNA-filled capsids in those phages (Chaikeeratisak et al., 2022). Time-lapse microscopy of the capsid fusion without any dyes present confirmed the temporal progression of capsid localization from membrane or cytosol, to the periphery of the nucleus, and then to the adjacent bouquet(s) (Figure S6E, see Video 7).

Cryo-FIB-ET confirmed that fully packaged capsids are arranged in a spherical formation, creating bouquets (Figures 6F and 6G). Consistent with our fluorescence and cryo-FIB-ET microscopy data of *Pseudomonas* phage bouquets (Chaikeeratisak et al., 2022), the interior of the observed bouquet is greatly depleted of host ribosomes compared to the surrounding cytosol. The majority of the

tails point to the inside of the bouquet and the capsids to the exterior, but a capsid localized inside the bouquet is observed (Figures 6F and 6G). Given the sizes of the bouquets (> 1.5 μm) compared to the thickness of FIB-milled lamellae (< 200 nm), we were unable to capture a bouquet in its entirety and ascertain its complete ultrastructure from our current cryo-FIB-ET dataset. Nevertheless, when combined with our fluorescence microscopy results, our cryo-FIB-ET data support the assembly of Goslar virions into double-layered bouquets at late stages of infection. Taken together, these data reveal that Goslar forms a distinctive type of prominent bouquet containing DNA-packed capsids within its center.

Discussion

Nucleus-forming jumbo phages rely on a tubulin-based cytoskeleton for their complex subcellular organization. In *Pseudomonas* jumbo phages 201φ2-1, ΦPA3, and ΦKZ, PhuZ forms a dynamic bipolar spindle that positions the phage nucleus at midcell and delivers capsids to the shell of the phage nucleus while rotating it (Chaikeeratisak et al., 2019, 2017a, 2017b; Erb et al., 2014; Kraemer et al., 2012). We have proposed that this conserved feature of nucleus-forming jumbo phage replication, while likely not essential for virus production, allows capsids to be distributed uniformly around the nucleus surface for efficient DNA packaging into capsids (Chaikeeratisak et al., 2019). Intracellular rotation in prokaryotes has only been reported for *Pseudomonas* infected by nucleus-forming jumbo phages, where a bipolar array of PhuZ filaments provides the forces necessary for rotation. Here we characterize Goslar infecting *E. coli* and demonstrate that this phage also has a complex replication cycle with both a nucleus-like compartment and a tubulin-based cytoskeleton that rotates it (Figure 7). Our findings regarding the Goslar phage nucleus are supported by our recent work showing that Goslar Chimallin shares high structural homology with

Chimallin from other jumbo phages like 201φ2-1, and assembles into a flexible lattice that is the primary component of the Goslar nuclear shell (Laughlin et al., 2022).

Surprisingly, Goslar PhuZ filaments assemble a vortex-like cytoskeletal structure in which filaments wrap around the entire phage nucleus and project radially toward the membrane (Figure 7). The orientation of the cytoskeletal vortex relative to the direction of rotation is consistent with the hypothesis that it generates force against the membrane to cause nucleus rotation, and expression of the PhuZ(D202A) mutant impairs both vortex formation and nucleus rotation. How can radially arranged filaments lead to intracellular rotation? If filaments emanate from the surface of the phage nucleus and are arranged radially around it, presumably no motion would occur if the forces they generated were perfectly balanced. A stochastic imbalance of forces is more likely to occur and this would lead to rotation in some direction. As a rotating nucleus tumbles inside the cell, it might appear to change directions relative to the long axis of the rod when visualized from a single plane. The process of rotation and consequential flow of cytoplasm can impose the alignment of filaments with the current direction of rotation, reinforcing the vortex array, as demonstrated for eukaryotic microtubules *in vitro* (Sumino et al., 2012; Suzuki et al., 2017).

A cytoskeletal vortex has not previously been described within any prokaryotes as far as we know. For eukaryotic microtubules, a self-organizing vortex array was demonstrated to spontaneously arise *in vitro* among purified microtubules with *Chlamydomonas* dynein c (Sumino et al., 2012) and in spatially confined droplets of *Xenopus* oocyte extract (Suzuki et al., 2017). The vortex of PhuZ filaments that organizes during Goslar infection visually resembles these *in vitro* microtubule vortex arrays. In eukaryotes, a vortex of cytoplasmic motion dependent on

microtubules and actin has been shown to be critical for development by driving cytoplasmic streaming in the eggs of several species as well as in plant cells (Schroeder and Battaglia, 1985; Serbus et al., 2005; Stein et al., 2021; Woodhouse and Goldstein, 2013). The eukaryotic cytoskeleton is also responsible for the rotation of the nucleus to align with cell polarity in motile cells, particularly fibroblasts (Fruleux and Hawkins, 2016; Gerashchenko et al., 2009; Kim et al., 2014; Kumar et al., 2014; Levy and Holzbaur, 2008; Maninová et al., 2014; Wu et al., 2011) and has been observed in a vortex-like arrangement during misalignment (Kumar et al., 2014). Goslar's PhuZ vortex that drives nucleus rotation demonstrates that cytoskeletal vortices are a conserved biological structure used by viruses and eukaryotes to coordinate complex cytoplasmic organization.

The results of this work suggest that the function of the vortex-like cytoskeletal network of PhuZ filaments is to drive phage nucleus rotation. Previous work on phage 201φ2-1 has demonstrated that inactivating the PhuZ cytoskeleton eliminates both nucleus rotation and capsid trafficking, thereby reducing the number of phage progeny produced by approximately 50% (Chaikeeratisak et al., 2019; Kraemer et al., 2012). In Goslar, the PhuZ cytoskeleton drives intracellular phage nucleus rotation and radially projecting filaments would be ideal conduits for capsid migration from the cell membrane to the surface of the phage nucleus, but further investigation must be done to determine whether Goslar PhuZ plays a role in capsid trafficking.

While this cytoskeletal vortex drives intracellular rotation, it did not appear to play a role in phage nucleus positioning. The Goslar phage nucleus is not positioned at the midcell as it is for the nucleus-forming *Pseudomonas* phages. Instead, it is positioned anywhere along the long axis of

the cell without significant enrichment of nucleus positioning at any given point along that axis. Expression of the PhuZ(D202A) mutant, which significantly reduces nucleus rotation, does not affect nucleus positioning. Thus, the main function of the Goslar PhuZ cytoskeleton may be to provide the driving forces for nuclear rotation and perhaps capsid delivery, rather than midcell positioning. It is not presently clear why some phages position the nucleus at midcell and Goslar does not. The midcell positioning in *Pseudomonas* phages may be a consequence of a bipolar spindle that facilitates rotation and it would have the added benefit of maintaining space between the surface of the phage nucleus and the cell membrane to allow the docking of capsids. In Goslar, with a vortex array instead of a bipolar spindle, the benefit of keeping space between the nucleus and the membrane is provided without midcell positioning.

At late stages of infection, Goslar virus particles accumulate in large spherical structures similar to the ones recently described in the nucleus-forming *Pseudomonas* phages and termed bouquets (Chaikeeratisak et al., 2022). In phage bouquets, virions are arranged in a sphere with capsids on the outside and tails facing inward. Goslar bouquets appeared similar to ΦPA3 bouquets except that Goslar's contained capsids located in the center of the phage bouquets rather than only around the outside, suggesting that Goslar bouquets are organized with internal capsids oriented inversely relative to the larger outer layer, with tails packed together (Figures 7D and 6D). The role of phage bouquets is currently unknown, and the fact that they are not always detected in phages ΦPA3 and ΦKZ, and are only rarely detected in phage 201φ2-1, suggests that they are not essential for phage replication (Chaikeeratisak et al., 2022). However, the discovery of prominent phage bouquets in Goslar, which is distantly related to the nucleus-forming *Pseudomonas* jumbo phages, suggests that bouquets offer an advantage to the phage.

The detailed characterization of the replication cycle of Goslar has brought to light a cytoskeletal vortex that drives phage nucleus rotation, which is a conserved process in the nucleus-forming jumbo phage replication cycle. This work also demonstrates that the replication mechanism involving a phage nucleus and spindle is widespread among phages infecting diverse hosts and that it likely confers a selective advantage since divergent strategies for rotation of the phage nucleus have evolved.

Limitations of the study

One limitation of this study is the use of fluorescent protein tags which can affect a protein's function. We have mitigated this by fusing the fluorophore to the terminus where it interferes the least in cases where this information is known. The N-terminus of Chimallin and PhuZ from *Pseudomonas* phages are known to be more amenable to tagging due to previous work. Another limitation is that GFP-tagged phage proteins expressed from a plasmid in the host bacterium are mixed with endogenous phage proteins normally expressed during infection. This caveat of our assays might have the greatest effect during expression of mutant proteins that are believed to act as dominant negatives, where the ratio of wild-type to mutant protein is unknown. Another caveat of fluorescent protein tags is their ability to oligomerize or otherwise associate with each other, which may cause artifacts in colocalization or the appearance of puncta. Finally, fluorescent imaging is restricted in its resolution. To counter this limitation, we corroborated certain findings with cryo-FIB-ET at high resolution.

Acknowledgements

This work was supported by the National Institutes of Health R01-GM129245 (to JP and EV) and R21-AI148814 (to KDC) and the National Science Foundation MRI grant NSF DBI 1920374 (to EV). EV is an investigator of the Howard Hughes Medical Institute. We acknowledge the use of the UC San Diego cryo-EM facility, which was built and equipped with funds from UC San Diego and an initial gift from the Agouron Institute. We thank Arshad Desai, Justin R. Meyer, and Amy M. Prichard for their helpful suggestions and comments on the manuscript.

Author Contributions

E.A.B., T.G.L., S.S., E.A., and J.L. conducted experiments and analyzed data. E.A.B. and J.P. conceptualized the original manuscript. J.W. provided the phage for study. E.A.B., T.G.L., E.A., J.W., K.D.C., E.V., and J.P. contributed to editing the manuscript.

Declaration of Interests

The authors declare no competing interests.

Figure 1. Goslar builds a phage nucleus separating DNA from translation and metabolism.

Goslar infecting *E. coli* MG1655 expressing fluorescent protein fusions (A-D) or APEC (E,F) for the indicated time. White scale bars are 1 μm. All fluorescent protein fusion expression was induced at 0.2 mM IPTG. Cells were stained with FM4-64 (4 μg/ml, membrane, magenta) and DAPI (2 μg/ml, DNA, cyan) (C,D). Fluorescence images were deconvolved using SoftWoRx 6.5.2. GFP-ChmA images are representative of at least 5 independent experiments.

(A) GFP-ChmA (gp189, yellow) 90 mpi. (B) GFP-ChmA and gp193-mCherry 60 mpi.

(C) 50S ribosomal protein L20 (RplT)-GFP, thymidylate kinase (TMK)-GFP, and soluble GFP, 60 minutes.

(D) GFP-ChmA, 30, 60, or 90 mpi.

(E) Slice through a deconvolved tomogram of a phage nucleus in a 90 mpi Goslar-infected APEC cell. Inset scale bar is 250 nm (1 - empty capsid, 2 - partially filled capsid, 3 - nearly full capsid). This tomogram is representative of 12 independent tomograms.

(F) Annotation of the tomogram shown in (E). Outer (red) and inner (pink) host cell membranes; phage nucleus shell (blue), capsids (green) and tails (cyan), 70S ribosomes (yellow).

Figure 2. Goslar PhuZ forms a vortex-like cytoskeletal array.

E. coli (MG1655) expressing GFP-PhuZ at 0.2 mM IPTG and infected with Goslar. Scale bars are 1 μm. GFP-PhuZ images are representative of at least 5 independent experiments.

(A) Cells at 30, 60, or 90 mpi prior to staining with FM4-64 and DAPI for 10 minutes.

(B) Cells at 90 and 120 mpi.

(C) Percentage of 30 mpi (n=75) or 60 mpi (n=114) cells with a GFP-PhuZ filament over 0.3 μm.

(D) Model of the PhuZ cytoskeletal vortex. PhuZ filaments (green) extend radially from the phage nucleus (blue) to the cell membrane (gold).

Figure 3. Colocalization experiments show the PhuZ cytoskeletal vortex wraps around the proteinaceous phage nucleus.

(A-C) *E. coli* (MG1655) co-expressing indicated fluorescent proteins induced with 0.2 mM IPTG and infected with Goslar. Scale bars are 1 μm. GFP-PhuZ images are representative of at least 3 independent experiments. Results are representative of at least 2 independent experiments.

(A) GFP-ChmA (yellow) and mCherry-PhuZ (magenta) in 90 mpi cells.

(B) mCherry-ChmA (magenta) and GFP-PhuZ (yellow) in 90 mpi cells.

(C) GFP-ChmA (yellow) and mCherry-PhuZ (magenta) in cells infected for 30, 60, or 90 minutes then dyed with DAPI (cyan).

(D) Distribution of DIC phage nuclei positions along the length of the cell (MG1655), in 0.05 fraction of the cell length bins. (30 mpi, n=35; 60 mpi, n=115; 90 mpi, n=122).

(E) 2D area of the DAPI-stained phage nucleus in MG1655 at 30 mpi (n=50), 60 mpi (n=114), and 90 mpi (n=121).

(F) Distribution of DIC phage nuclei positions along the length of the APEC cell, in 0.05 fraction of cell length bins. (30 mpi; n=96, 60 mpi; n=105, 90 mpi; n=114).

(G) 2D area of the DAPI-stained phage nucleus in APEC at 30 mpi (n=115), 60 mpi (n=120), and 90 mpi (n=145).

Figure 4. The Goslar phage nucleus rotates.

E. coli (MG1655) expressing the indicated fusion protein induced with 0.2 mM IPTG and infected with Goslar**.** Scale bars are 1 μm.

(A) Time-lapse of the phage nucleus every 4 seconds for 20 seconds in cells expressing GFP-ChmA (white) at 65 mpi. Yellow arrowhead and bracket are markers for following rotation. Also see Video 1.

(B) DIC time-lapse every 4 seconds for 20 seconds in 60 mpi cells. Results are representative of at least 3 independent experiments. Also see Video 2.

(C) Linear velocity of nucleus rotation measured from DIC time-lapse, averaging 50 nm/s (n=20), red dotted line, individual measurements shown as gray lines.

(D) Model of ΦKZ phage nucleus rotation by bipolar PhuZ spindle (top) and Goslar phage nucleus rotation by PhuZ cytoskeletal vortex (bottom). Arrows indicate the direction of forces applied to the phage nucleus and direction of rotation.

(E) GFP imaging coupled with DIC time-lapse every 4 seconds on cells expressing GFP-PhuZ (yellow, left panels); yellow arrowhead indicates DIC-density to follow for rotation, red curved arrows in final panels indicate direction of rotation (CCW top cell, CW bottom cell). Results are representative of 2 independent experiments.

Figure 5. Mutant PhuZ(D202A) disrupts filament formation and nucleus rotation.

(A) *E. coli* expressing GFP-PhuZ(D202A) at 0.2 mM IPTG and infected by Goslar for 60 minutes before being stained with FM4-64 and DAPI. Scale bar is 1 μm.

(B) DIC time-lapse every 4 seconds for 36 seconds on *E. coli* expressing GFP-PhuZ(D202A) at 0.2 mM IPTG and infected by Goslar for 60 minutes. Same scale as (A). Results of (A) and (B) are representative of 3 independent experiments. Also see Videos 3 and 4.

(C) Percentage of the infected cells at 60 mpi that had a rotating nucleus with any amount of progressive movement imaged by DIC time-lapse for *E. coli* with no plasmid (MG1655, n=105) or cells expressing GFP-PhuZ (n=164) or GFP-PhuZ(D202A) (n=101) (*unpaired t-test,* * p value = 0.04, **** p value <0.0001).

(D) Linear velocity of the most progressively rotating nuclei at 60 mpi by DIC time-lapse for *E. coli* with no plasmid (MG1655, n=20) or cells expressing GFP-PhuZ (n=20) or GFP-PhuZ(D202A) (n=23). Violin plot generated and unpaired t tests performed using GraphPad Prism 9 (*unpaired t-test,* ns - p value >0.05, **** p value <0.0001).

Figure 6. Goslar capsids migrate from the cytoplasm, surround the phage nucleus, and form phage bouquets.

Goslar infecting *E. coli* MG1655 (B) or MG1655 expressing the putative capsid protein (gp41) fused to GFP (yellow) (A,E) or APEC (C,F,G) for the indicated time. White scale bars are 1 μm. All fluorescent protein fusion expression was induced at 0.2 mM IPTG. Results are representative of at least 3 independent experiments.

(A) Infected cells at 90 mpi. Bouquets are found around the phage nucleus (left panels), in adjacent bouquets (middle panels), and filling more of the cytoplasm (right panels).

(B) 90 mpi MG1655 cells stained with 10 μg/ml DAPI for 30 minutes at room temperature. White arrowheads indicate faint bouquets.

(C) APEC grown with 200 ng/ml DAPI for 90 minutes then infected with Goslar for 90 minutes. Large, brightly fluorescent phage bouquets are formed. See Videos 5 and 6 for 3D reconstructions of left panels.

(D) Model of Goslar phage bouquet organization with tails packed together.

(E) MG1655 expressing capsid-GFP (yellow) and infected with Goslar for 30, 40, 50, 60, 70, or 90 minutes before being stained with FM4-64 (magenta) and DAPI (cyan). Also see Video 7.

(F) Slice through a deconvolved tomogram of a phage bouquet in a Goslar-infected APEC cell at 90 mpi. Inset scale bar is 250 nm.

(G) Annotation of the tomogram shown in (F). Outer (red) and inner (pink) host cell membranes, phage nucleus shell (blue), capsids (green), tails (cyan), 70S ribosomes (yellow).

Figure 7. Model of the Goslar infection cycle.

(A) The Goslar phage injects its DNA into an *E. coli* cell and the formation of a shell begins.

(B) The shell grows in size as DNA replicates inside and the PhuZ vortex begins to form. Capsids form near the periphery of the cell and migrate towards the phage nucleus, possibly by trafficking along PhuZ filaments as we have demonstrated for *Pseudomonas* phages (Chaikeeratisak et al., 2019).

(C) The PhuZ vortex is fully formed, wrapping around and rotating the phage nucleus. Capsids dock on the nuclear shell to be filled with DNA prior to localizing to the adjacent bouquets.

(D) Large bouquets form with internally localized capsids on either one side or both sides of the phage nucleus.

(E) Final assembly of the progeny virions is completed as they fill the cell in a more disordered fashion.

(F) Lysis of the *E. coli* cell is achieved, releasing the progeny virions to find the next host.

STAR METHODS

Resource Availability

Lead contact

Further information and requests for resources and reagents should be directed to and will be fulfilled by the lead contact, Joe Pogliano (jpogliano@ucsd.edu).

Materials availability

This study did not generate new unique reagents.

Data and code availability

- Original microscopy images have been deposited at Mendeley and are publicly available as of the date of publication. DOIs are listed in the key resources table.
- This paper does not report any original code.
- Any additional information required to reanalyze the data reported in this paper is available from the lead contact upon request.

Experimental Model and Subject Details

Growth conditions and bacteriophage preparation

Bacterial strains used in this study are listed in the Key Resources Table. The *Escherichia coli* strain APEC 2248 (APEC, serotype O78++) is an avian pathogen. It is closely related to *E. coli* K-12, approximately 99% identical (Dziva et al., 2013). *E. coli* strains APEC and MG1655 were grown on Luria-Bertani (LB) plates containing 10 g Bacto-Tryptone, 5 g NaCl, 5 g Bacto-yeast extract, 16 g agar in 1 L ddH_2O and incubated at 37°C overnight. Liquid cultures were obtained by inoculation of LB broth with one colony of *E. coli* from an LB plate. Lysates for Goslar were obtained from Johannes Wittmann at the DSMZ and were amplified by adding 15 µl high titer

phage lysate to 300 µl APEC at OD_{600} 0.5, incubating at 37°C for 30 minutes, then adding 300 µl LB broth, plating 200 µl of the suspension onto each of 3 LB plates and incubating at 37°C overnight. 15 ml of Phage Buffer (PB) containing 10 mM Tris (pH 7.5), 10 mM $MgSO_4$, 68 mM NaCl, and 1 mM $CaCl_2$ was chilled on ice before 5 ml was added to each plate and left to soak at room temperature. After 4 hours, 3 ml of PB was added to each plate and after 2 more hours, the buffer was drawn off into a single tube. The lysate was clarified by pelleting the bacteria at 3220 x g for 10 minutes. The supernatant was filtered through a 0.45 µm Corning membrane filter by syringe. 5 drops of chloroform from a pasteur pipette were added to the 10 ml lysate and shaken by hand for 1 minute. The mixture was spun at 3220 x g for 5 minutes and the aqueous phase containing the phage was removed to a clean tube and stored at 4°C.

Plasmid constructions and bacterial transformation

Fluorescent-tagged phage proteins were synthesized and cloned by restriction with SacI and SalI of pDSW206 by Genscript and delivered as lyophilized plasmid. The plasmids were hydrated at ~0.2 g/L with Tris-EDTA buffer and diluted 1:10 with ddH_2O. Electroporation competent DH5α and MG1655 cells were prepared by washing with 10% glycerol and stored at -80°C. 30-50 µl of competent cells was combined with 1 µl of diluted plasmid and electroporated with 1.8 kV then incubated at 30°C in SOC media for 30-60 minutes before plating on LB with 100 µg/ml ampicillin and incubating overnight at 37°C.

Method Details

Single cell infection assay

E. coli strains containing a plasmid with fluorescent-tagged phage protein(s) were grown on 1% agarose pads supplemented with 25% LB and the desired IPTG concentration to induce protein expression. Cells were obtained from overnight incubation at 37°C on an LB plate with 100 μg/ml ampicillin. A colony was resuspended in 25% LB to an OD_{600} of ~0.35 then 8 μl was spotted on the imaging pad and spread with the bottom of an eppendorf tube. Wild-type *E. coli* was grown without ampicillin or IPTG. The imaging pad was then incubated at 37°C for 1.5 hours without a coverslip in a humidor. 6 μl of Goslar lysate was added to the agarose pads and spread as before, then further incubated at 37°C to allow phage infection to proceed. At the desired time point, the slide was placed at room temperature and spotted with 7 μl of dye mix (2 μg/ml DAPI, 4 μg/ml FM4-64, 25% LB). Once dry after ~5 minutes, a coverslip was put on the agarose pad and fluorescent microscopy was initiated. Data of static images and time-lapse imaging were collected and processed as described below.

Live cell static image and time-lapse fluorescence microscopy

The DeltaVision Elite Deconvolution microscope (Applied Precision, Issaquah, WA, USA) was used to visualize the live cells. DIC imaging was performed with the DIC prism removed from the light path which provided enhanced visualization of the phage nucleus. For static images, the cells were imaged with 12-15 slices in the Z-axis at 0.15 μm increments. For long time-lapse, imaging pads were prepared and infected as above and 30 minutes after the addition of Goslar, pads were coverslipped without dyes. The environmental control unit surrounding the microscope warmed the imaging space to 35°C. Fields adequate for imaging were marked and time-lapse imaging

began within 10 minutes, with Ultimate Focus utilized. For short time-lapse, infections proceeded at 37°C for the indicated time before being coverslipped and imaged at room temperature one field at a time using Ultimate Focus. Images were processed by the aggressive deconvolution algorithm in the DeltaVision SoftWoRx 6.5.2 Image Analysis Program. Further image analysis and processing was performed in FIJI version 2.1.0/1.53c. Figure images were adjusted and layered in Adobe Photoshop.

Cryo-electron tomography sample preparation

Ten agarose pads for infection were prepared as above (1% agarose, 25% LB) and spotted with 10 µl of APEC cells at an OD_{600} of ~0.35 then incubated at 37°C for 1.5 hours in a humidor. 10 µl of Goslar lysate from the DSMZ was added and spread on each pad then incubated for another 1.5 hours until being removed to room temperature for cell collection. Infected cells were removed from the pads by addition of 25 µl of 25% LB and gentle scraping with the bottom of an eppendorf tube. All 10 pads were collected into one tube and after a portion was aliquoted, the remainder was centrifuged at 6000 x g for 45 seconds, resuspended with ¼ volume of the supernatant, and a portion of that was diluted 1:1 in supernatant. Samples were delivered for plunging 20-30 minutes after removal from 37°C which significantly slows infection progression.

Cryo-focused ion beam milling and electron tomography

Infected cells were prepared as described above and at approximately 90 minutes post infection, 4-7 µl of cells were deposited on R2/1 Cu 200 grids (Quantifoil) that had been glow-discharged for 1 min at 0.19 mbar and 20 mA in a PELCO easiGlow device shortly before use. Grids were mounted in a custom-built manual plunging device (Max Planck Institute of Biochemistry,

Martinsried) and excess liquid was blotted with filter paper from the backside of the grid for 5-7 seconds prior to freezing in a 50:50 ethane:propane mixture (Airgas) cooled by liquid nitrogen.

Grids were mounted into modified Autogrids (TFS) compatible with cryo-focused ion beam milling. Samples were loaded into an Aquilos 2 cryo-focused ion beam/scanning electron microscope (TFS) and milled to yield lamellae following published procedures for bacterial samples (Lam and Villa, 2021).

Milled specimens were imaged with a Titan Krios G3 transmission electron microscope (TFS) operated at 300 kV and equipped with a K2 directed electron detector (Gatan) mounted post Quantum 968 LS imaging filter (Gatan). The microscope was operated in EFTEM mode with a slit-width of 20 eV and using a 70 µm objective aperture. Automated data acquisition was performed using SerialEM-v3.8b11 (Mastronarde, 2005) and all recorded images were collected using the K2 in counting mode.

Tilt-series were acquired at either 4.27 Å and 5.34 Å per pixel. For the higher magnification tilt-series, images were acquired over a nominal range of +/-60^{o} in 2^{o} steps following a dose-symmetric scheme (Hagen et al., 2017) with a per-tilt fluence of 2.6 $e^{-} \cdot Å^{-2}$ and total of ~ 160 $e^{-} \cdot Å^{-2}$ per tilt-series. Lower magnification tilt-series were acquired similarly, but using a 1.5^{o} tilt-step and per-tilt fluence of 1.8 $e^{-} \cdot Å^{-2}$. Target defocus values were set for between -5 and -6 µm.

Image processing and analysis of cryo-electron tomography data

Tilt-movies were corrected for whole-frame motion using Warp-v1.09 (Tegunov and Cramer, 2019) and aligned via patch-tracking using Etomo (IMOD-v4.10.28) (Mastronarde and Held, 2017). Tilt-series CTF parameters were estimated and tomograms reconstructed with exposure-filtering and CTF-correction using Warp-v1.09. For general visualization and membrane segmentation, tomograms were reconstructed using Warp's deconvolution filter applied at default settings and downsampled to 20 Å and 25 Å per pixel from the original 4.27 Å and 5.34 Å pixel sizes, respectively.

Segmentation of host cell membranes and the phage nucleus perimeter from representative tomograms was performed by first coarsely segmenting using TomoSegMemTV (Martinez-Sanchez et al., 2014) followed by manual patching with Amira-v6.7 (TFS). Ribosomes, capsids, and tails were segmented using subtomogram analysis. For ribosomes, approximately 200 particles were manually selected from the respective tomograms and used to generate an *ab initio* reference using Warp-v1.09 and Relion-v3.1.1 (Scheres, 2012) following conventional procedures (Bharat and Scheres, 2016; Tegunov and Cramer, 2019). The references were used for template-matching with Warp-v1.09 against their respective tomograms. Template-matching results were curated to remove obvious false-positives (e.g., picks outside cell boundaries and cell membranes, etc.). Curated picks were aligned and classified using Relion-v3.1.1 to remove additional false-positives and refine their positions in the tomogram. For capsids, all particles were manually picked. Reference-generation and alignment of capsids was performed while enforcing icosahedral symmetry with Relion-v3.1.1 (despite the capsids possessing C5 symmetry) in order to promote convergence from the low number of particles. For the phage tails, the start and end points along the filament axis were defined manually and used to generate over-sampled filament models in

Dynamo-v1.1514 (Castaño-Díez et al., 2017, 2012). An initial reference for the tail was generated using Dynamo-v1.1514 from two full-length tails with clearly defined polarity. The resulting reference displayed apparent C6 symmetry, which was enforced for the alignment of all tails from a given tomogram using Dynamo-v1.1514 and Relion-v3.1.1. All interconversions of metadata between Warp/Relion and Dynamo formats were performed using scripts from the dynamo2m-v0.2.2 package (Burt et al., 2021). Final averages were placed back in the reference-frame of their respective tomograms using *dynamo_table_place*. Figures of the segmentation models were prepared using ChimeraX-v1.2.1(Pettersen et al., 2021).

Construction of PhuZ and shell phylogenetic trees

PSI-BLAST queried ΦKZ PhuZ (gp039) and shell (gp054). All phage-encoded hits were pulled and only those with both a PhuZ and a shell were aligned by MUSCLE and used to construct the trees in MEGA X (10.2.6) (Kumar et al., 2018; Stecher et al., 2020). The evolutionary history was inferred using the Neighbor-Joining method and bootstrapped with 1000 replicates. Evolutionary distances were calculated using the Poisson correction method.

Quantification and Statistical Analysis

To quantify filaments of GFP-PhuZ or GFP-PhuZ(D202A), non-deconvolved DeltaVision image files were opened in FIJI version 2.1.0/1.53c using the Bio-formats importer. Images were automatically scaled at 15.456 pixels per μm and filaments were measured in the GFP channel at the slice containing the filament.

For the percentage of the infected population that had a rotating nucleus, an A/B test was

performed and a p value < 0.05 was the threshold for statistical significance.

Measurement of the linear velocity of nucleus rotation was performed on DIC images taken every 4 seconds. Dark protrusions on the surface of the phage nucleus were traced by hand over 12 second intervals (3 images) using the segmented line tool and their lengths recorded. Total distance traveled by points on the nuclear surface was divided by total time (120 seconds) and averaged with standard deviation calculated. Data is displayed as a violin plot produced in GraphPad Prism 9.2.0 for Mac OS X. An unpaired t-test was performed to obtain p values ($p < 0.05$, significant).

Supplemental Videos

Video 1. GFP-tagged Goslar nucleus rotates in MG1655. Related to Figure 4.

Live cell GFP time-lapse of a Goslar nucleus at 65 mpi in the strain expressing GFP-shell. Image interval is 2 seconds with a total elapsed time of 30 seconds. Scale bar is 1 μm.

Video 2. Goslar nucleus rotates without tagged proteins present. Related to Figure 4.

Live cell DIC time-lapse of MG1655 with no plasmid. Image interval is 2 seconds with a total elapsed time of 60 seconds. Scale bar is 1 μm.

Videos 3 and 4. Goslar nucleus no longer rotates in the presence of GFP-PhuZ(D202A). Related to Figure 5.

Live cell DIC time-lapse of MG1655 expressing GFP-PhuZ(D202A) and infected with Goslar for 75 minutes (Video 3) or 85 minutes (Video 4). Image interval is 4 seconds with a total elapsed time of 80 seconds (Video 3) or 160 seconds (Video 4). Scale bars are 1 μm.

Videos 5 and 6. Goslar bouquets can contain DNA-filled capsids in the interior. Related to Figure 6.

3D reconstruction (FIJI – max intensity – interpolated) of DAPI-stained Goslar infections in live cells after 90 mpi. Scale bars are 1 μm.

Video 7. Goslar capsids migrate from the cell periphery to the nucleus to adjacent bouquets. Related to Figure 6.

Live cell GFP time-lapse of MG1655 expressing capsid-GFP and infected with Goslar for 10 minutes prior to imaging. DIC images are provided at the beginning and end of the time-lapse for reference of cell boundaries and nucleus position. GFP images begin at 40 mpi with an interval of 2 minutes and a total elapsed time of 40 minutes.

References

Aylett, C.H.S., Izoré, T., Amos, L.A., Löwe, J., 2013. Structure of the tubulin/FtsZ-like protein TubZ from Pseudomonas bacteriophage ΦKZ. J. Mol. Biol. 425, 2164–2173.

Bharat, T.A.M., Scheres, S.H.W., 2016. Resolving macromolecular structures from electron cryo-tomography data using subtomogram averaging in RELION. Nat. Protoc. 11, 2054–2065.

Burt, A., Gaifas, L., Dendooven, T., Gutsche, I., 2021. Tools enabling flexible approaches to high-resolution subtomogram averaging. bioRxiv.

Castaño-Díez, D., Kudryashev, M., Arheit, M., Stahlberg, H., 2012. Dynamo: a flexible, user-friendly development tool for subtomogram averaging of cryo-EM data in high-performance computing environments. J. Struct. Biol. 178, 139–151.

Castaño-Díez, D., Kudryashev, M., Stahlberg, H., 2017. Dynamo Catalogue: Geometrical tools and data management for particle picking in subtomogram averaging of cryo-electron tomograms. J. Struct. Biol. 197, 135–144.

Ceyssens, P.J., Minakhin, L., Van den Bossche, A., Yakunina, M., Klimuk, E., Blasdel, B., De Smet, J., Noben, J.-P., Bläsi, U., Severinov, K., Lavigne, R., 2014. Development of giant bacteriophage ϕKZ is independent of the host transcription apparatus. J. Virol. 88, 10501–10510.

Chaikeeratisak, V., Birkholz, E.A., Pogliano, J., 2021a. The Phage Nucleus and PhuZ Spindle: Defining Features of the Subcellular Organization and Speciation of Nucleus-Forming Jumbo Phages. Front. Microbiol. 12, 641317.

Chaikeeratisak, V., Birkholz, E.A., Prichard, A.M., Egan, M.E., Mylvara, A., Nonejuie, P., Nguyen, K.T., Sugie, J., Meyer, J.R., Pogliano, J., 2021b. Viral speciation through subcellular genetic isolation and virogenesis incompatibility. Nat. Commun. 12, 342.

Chaikeeratisak, V., Khanna, K., Nguyen, K.T., Egan, M.E., Enustun, E., Armbruster, E., Lee, J., Pogliano, K., Villa, E., Pogliano, J., 2022. Subcellular organization of viral particles during maturation of nucleus-forming jumbo phage. Science Advances 8.

Chaikeeratisak, V., Khanna, K., Nguyen, K.T., Sugie, J., Egan, M.E., Erb, M.L., Vavilina, A., Nonejuie, P., Nieweglowska, E., Pogliano, K., Agard, D.A., Villa, E., Pogliano, J., 2019. Viral Capsid Trafficking along Treadmilling Tubulin Filaments in Bacteria. Cell 177, 1771–1780.e12.

Chaikeeratisak, V., Nguyen, K., Egan, M.E., Erb, M.L., Vavilina, A., Pogliano, J., 2017a. The Phage Nucleus and Tubulin Spindle Are Conserved among Large Pseudomonas Phages. Cell Rep. 20, 1563–1571.

Chaikeeratisak, V., Nguyen, K., Khanna, K., Brilot, A.F., Erb, M.L., Coker, J.K.C., Vavilina, A., Newton, G.L., Buschauer, R., Pogliano, K., Villa, E., Agard, D.A., Pogliano, J., 2017b. Assembly of a nucleus-like structure during viral replication in bacteria. Science 355, 194–197.

Charman, M., Weitzman, M.D., 2020. Replication Compartments of DNA Viruses in the Nucleus: Location, Location, Location. Viruses 12.

Danilova, Y.A., Belousova, V.V., Moiseenko, A.V., Vishnyakov, I.E., Yakunina, M.V., Sokolova, O.S., 2020. Maturation of Pseudo-Nucleus Compartment in P. aeruginosa, Infected with Giant phiKZ Phage. Viruses 12.

Dziva, F., Hauser, H., Connor, T.R., van Diemen, P.M., Prescott, G., Langridge, G.C., Eckert, S., Chaudhuri, R.R., Ewers, C., Mellata, M., Mukhopadhyay, S., Curtiss, R., 3rd, Dougan, G.,

Wieler, L.H., Thomson, N.R., Pickard, D.J., Stevens, M.P., 2013. Sequencing and functional annotation of avian pathogenic Escherichia coli serogroup O78 strains reveal the evolution of E. coli lineages pathogenic for poultry via distinct mechanisms. Infect. Immun. 81, 838–849.
Erb, M.L., Kraemer, J.A., Coker, J.K.C., Chaikeeratisak, V., Nonejuie, P., Agard, D.A., Pogliano, J., 2014. A bacteriophage tubulin harnesses dynamic instability to center DNA in infected cells. Elife 3.
Fruleux, A., Hawkins, R.J., 2016. Physical role for the nucleus in cell migration. J. Phys. Condens. Matter 28, 363002.
Gerashchenko, M.V., Chernoivanenko, I.S., Moldaver, M.V., Minin, A.A., 2009. Dynein is a motor for nuclear rotation while vimentin IFs is a "brake." Cell Biol. Int. 33, 1057–1064.
Hagen, W.J.H., Wan, W., Briggs, J.A.G., 2017. Implementation of a cryo-electron tomography tilt-scheme optimized for high resolution subtomogram averaging. J. Struct. Biol. 197, 191–198.
Kim, D.H., Cho, S., Wirtz, D., 2014. Tight coupling between nucleus and cell migration through the perinuclear actin cap. J. Cell Sci. 127, 2528–2541.
Korf, I.H.E., Meier-Kolthoff, J.P., Adriaenssens, E.M., Kropinski, A.M., Nimtz, M., Rohde, M., van Raaij, M.J., Wittmann, J., 2019. Still Something to Discover: Novel Insights intoEscherichia coli Phage Diversity and Taxonomy. Viruses 11.
Kraemer, J.A., Erb, M.L., Waddling, C.A., Montabana, E.A., Zehr, E.A., Wang, H., Nguyen, K., Pham, D.S.L., Agard, D.A., Pogliano, J., 2012. A phage tubulin assembles dynamic filaments by an atypical mechanism to center viral DNA within the host cell. Cell 149, 1488–1499.
Krylov, V., Bourkaltseva, M., Pleteneva, E., Shaburova, O., Krylov, S., Karaulov, A., Zhavoronok, S., Svitich, O., Zverev, V., 2021. Phage phiKZ-The First of Giants. Viruses 13.
Kumar, A., Maitra, A., Sumit, M., Ramaswamy, S., Shivashankar, G.V., 2014. Actomyosin contractility rotates the cell nucleus. Sci. Rep. 4, 3781.
Kumar, S., Stecher, G., Li, M., Knyaz, C., Tamura, K., 2018. MEGA X: Molecular Evolutionary Genetics Analysis across Computing Platforms. Mol. Biol. Evol. 35, 1547–1549.
Lam, V., Villa, E., 2021. Practical Approaches for Cryo-FIB Milling and Applications for Cellular Cryo-Electron Tomography. Methods Mol. Biol. 2215, 49–82.
Larsen, R.A., Cusumano, C., Fujioka, A., Lim-Fong, G., Patterson, P., Pogliano, J., 2007. Treadmilling of a prokaryotic tubulin-like protein, TubZ, required for plasmid stability in Bacillus thuringiensis. Genes Dev. 21, 1340–1352.
Laughlin, T.G., Deep, A., Prichard, A.M., Seitz, C., Gu, Y., Enustun, E., Suslov, S., Khanna, K., Birkholz, E.A., Armbruster, E., Andrew McCammon, J., Amaro, R.E., Pogliano, J., Corbett, K.D., Villa, E., 2022. Architecture and self-assembly of the jumbo bacteriophage nuclear shell. bioRxiv.
Lecoutere, E., Ceyssens, P.J., Miroshnikov, K.A., Mesyanzhinov, V.V., Krylov, V.N., Noben, J.-P., Robben, J., Hertveldt, K., Volckaert, G., Lavigne, R., 2009. Identification and comparative analysis of the structural proteomes of phiKZ and EL, two giant Pseudomonas aeruginosa bacteriophages. Proteomics 9, 3215–3219.
Levy, J.R., Holzbaur, E.L.F., 2008. Dynein drives nuclear rotation during forward progression of motile fibroblasts. J. Cell Sci. 121, 3187–3195.
Malone, L.M., Warring, S.L., Jackson, S.A., Warnecke, C., Gardner, P.P., Gumy, L.F., Fineran,

P.C., 2020. A jumbo phage that forms a nucleus-like structure evades CRISPR-Cas DNA targeting but is vulnerable to type III RNA-based immunity. Nat Microbiol 5, 48–55.
Maninová, M., Iwanicki, M.P., Vomastek, T., 2014. Emerging role for nuclear rotation and orientation in cell migration. Cell Adh. Migr. 8, 42–48.
Martinez-Sanchez, A., Garcia, I., Asano, S., Lucic, V., Fernandez, J.J., 2014. Robust membrane detection based on tensor voting for electron tomography. J. Struct. Biol. 186, 49–61.
Mastronarde, D.N., 2005. Automated electron microscope tomography using robust prediction of specimen movements. J. Struct. Biol. 152, 36–51.
Mastronarde, D.N., Held, S.R., 2017. Automated tilt series alignment and tomographic reconstruction in IMOD. J. Struct. Biol. 197, 102–113.
Mendoza, S.D., Nieweglowska, E.S., Govindarajan, S., Leon, L.M., Berry, J.D., Tiwari, A., Chaikeeratisak, V., Pogliano, J., Agard, D.A., Bondy-Denomy, J., 2020. A bacteriophage nucleus-like compartment shields DNA from CRISPR nucleases. Nature 577, 244–248.
Mesyanzhinov, V.V., Robben, J., Grymonprez, B., Kostyuchenko, V.A., Bourkaltseva, M.V., Sykilinda, N.N., Krylov, V.N., Volckaert, G., 2002. The genome of bacteriophage phiKZ of Pseudomonas aeruginosa. J. Mol. Biol. 317, 1–19.
Monson, R., Foulds, I., Foweraker, J., Welch, M., Salmond, G.P.C., 2011. The Pseudomonas aeruginosa generalized transducing phage phiPA3 is a new member of the phiKZ-like group of "jumbo" phages, and infects model laboratory strains and clinical isolates from cystic fibrosis patients. Microbiology 157, 859–867.
Nguyen, K.T., Sugie, J., Khanna, K., Egan, M.E., Birkholz, E.A., Lee, J., Beierschmitt, C., Villa, E., Pogliano, J., 2021. Selective transport of fluorescent proteins into the phage nucleus. PLoS One 16, e0251429.
Orekhova, M., Koreshova, A., Artamonova, T., Khodorkovskii, M., Yakunina, M., 2019. The study of the phiKZ phage non-canonical non-virion RNA polymerase. Biochem. Biophys. Res. Commun. 511, 759–764.
Pettersen, E.F., Goddard, T.D., Huang, C.C., Meng, E.C., Couch, G.S., Croll, T.I., Morris, J.H., Ferrin, T.E., 2021. UCSF ChimeraX: Structure visualization for researchers, educators, and developers. Protein Sci. 30, 70–82.
Scheres, S.H.W., 2012. RELION: implementation of a Bayesian approach to cryo-EM structure determination. J. Struct. Biol. 180, 519–530.
Schroeder, T.E., Battaglia, D.E., 1985. "Spiral asters" and cytoplasmic rotation in sea urchin eggs: induction in Strongylocentrotus purpuratus eggs by elevated temperature. J. Cell Biol. 100, 1056–1062.
Serbus, L.R., Cha, B.J., Theurkauf, W.E., Saxton, W.M., 2005. Dynein and the actin cytoskeleton control kinesin-driven cytoplasmic streaming in Drosophila oocytes. Development 132, 3743–3752.
Sokolova, M.L., Misovetc, I., Severinov, K., V., 2020. Multisubunit RNA Polymerases of Jumbo Bacteriophages. Viruses 12.
Stecher, G., Tamura, K., Kumar, S., 2020. Molecular Evolutionary Genetics Analysis (MEGA) for macOS. Mol. Biol. Evol. 37, 1237–1239.
Stein, D.B., De Canio, G., Lauga, E., Shelley, M.J., Goldstein, R.E., 2021. Swirling Instability of the Microtubule Cytoskeleton. Phys. Rev. Lett. 126, 028103.
Sumino, Y., Nagai, K.H., Shitaka, Y., Tanaka, D., Yoshikawa, K., Chaté, H., Oiwa, K., 2012. Large-scale vortex lattice emerging from collectively moving microtubules. Nature 483, 448–452.

Suzuki, K., Miyazaki, M., Takagi, J., Itabashi, T., Ishiwata, S., 2017. Spatial confinement of active microtubule networks induces large-scale rotational cytoplasmic flow. Proc. Natl. Acad. Sci. U. S. A. 114, 2922–2927.
Tegunov, D., Cramer, P., 2019. Real-time cryo-electron microscopy data preprocessing with Warp. Nat. Methods 16, 1146–1152.
Thomas, J.A., Rolando, M.R., Carroll, C.A., Shen, P.S., Belnap, D.M., Weintraub, S.T., Serwer, P., Hardies, S.C., 2008. Characterization of Pseudomonas chlororaphis myovirus 201varphi2-1 via genomic sequencing, mass spectrometry, and electron microscopy. Virology 376, 330–338.
Thomas, J.A., Weintraub, S.T., Hakala, K., Serwer, P., Hardies, S.C., 2010. Proteome of the Large Pseudomonas Myovirus 201φ2-1: Delineation of Proteolytically Processed Virion Proteins. Mol. Cell. Proteomics 9, 940–951.
Thomas, J.A., Weintraub, S.T., Wu, W., Winkler, D.C., Cheng, N., Steven, A.C., Black, L.W., 2012. Extensive proteolysis of head and inner body proteins by a morphogenetic protease in the giant Pseudomonas aeruginosa phage φKZ. Mol. Microbiol. 84, 324–339.
Weintraub, S.T., Mohd Redzuan, N.H., Barton, M.K., Md Amin, N.A., Desmond, M.I., Adams, L.E., Ali, B., Pardo, S., Molleur, D., Wu, W., Newcomb, W.W., Osier, M.V., Black, L.W., Steven, A.C., Thomas, J.A., 2019. Global proteomic profiling of Salmonella infection by a giant phage. J. Virol. 93.
Woodhouse, F.G., Goldstein, R.E., 2013. Cytoplasmic streaming in plant cells emerges naturally by microfilament self-organization. Proc. Natl. Acad. Sci. U. S. A. 110, 14132–14137.
Wu, J., Lee, K.C., Dickinson, R.B., Lele, T.P., 2011. How dynein and microtubules rotate the nucleus. J. Cell. Physiol. 226, 2666–2674.
Yakunina, M., Artamonova, T., Borukhov, S., Makarova, K.S., Severinov, K., Minakhin, L., 2015. A non-canonical multisubunit RNA polymerase encoded by a giant bacteriophage. Nucleic Acids Res. 43, 10411–10420.
Zehr, E.A., Kraemer, J.A., Erb, M.L., Coker, J.K.C., Montabana, E.A., Pogliano, J., Agard, D.A., 2014. The structure and assembly mechanism of a novel three-stranded tubulin filament that centers phage DNA. Structure 22, 539–548.

Key resources table

REAGENT or RESOURCE	SOURCE	IDENTIFIER
Bacterial and virus strains		
E. coli MG1655	CGSC	CGSC 6300
E. coli APEC 2248 (APEC)	DSMZ	DSM 103255
NEB5-alpha competent E. coli	New England Biolabs	Cat#C2987H
vB_EcoM_Goslar	Johannes Wittmann (DSMZ) [29]	DSM 104658
Chemicals, peptides, and recombinant proteins		
DAPI (4',6-Diamidino-2-Phenylindole,Dihydrochloride)	Thermo Fisher Scientific	Cat#D1306
FM 4-64	Thermo Fisher Scientific	Cat#T13320
Ampicillin	Thermo Fisher Scientific	Cat#BP1760-25
Isopropylthio-β-galactoside (IPTG)	Teknova	Cat#I3305
Deposited data		
Mendeley Data Set	This study	10.17632/skf8x9kkz8.1
Recombinant DNA		
pDSW206 plasmid	David Weiss [44]	N/A
Table S1		
Software and algorithms		
DeltaVision SoftWoRx 6.5.2	GE HealthCare	incelldownload.gehealthcare.com/bin/download_data/SoftWoRx/7.0.0/SoftWoRx.htm
FIJI ver 2.1.0/1.53c	ImageJ [45]	imagej.net/software/fiji/
GraphPad Prism version 9.2.0 for Mac OS X	GraphPad Software, San Diego, California USA.	www.graphpad.com
MEGA X 10.2.6	MEGA [46,47]	www.megasoftware.net
Microsoft Excel	Microsoft Office	www.microsoft.com/en-us/microsoft-365/excel
Microsoft Powerpoint	Microsoft Office	www.microsoft.com/en-us/microsoft-365/powerpoint
Adobe Photoshop	Adobe	www.adobe.com/products/photoshop.html
Adobe Illustrator	Adobe	www.adobe.com/products/illustrator.html
SerialEM ver 3.8b11	[48]	bio3d.colorado.edu/SerialEM/
Warp ver 1.09	[49]	www.warpem.com/warp/
IMOD Package ver 4.10.28	[50]	bio3d.colorado.edu/imod/
Matlab 2019b	MathWorks	www.mathworks.com
Dynamo ver 1.1514	[51]	wiki.dynamo.biozentrum.unibas.ch
dynamo2m ver 0.2.2	[52]	github.com/alisterburt/dynamo2m
RELION ver 3.1.1	[53,54]	relion.readthedocs.io/en/release-3.1/
TomoSegMemTV	[55]	sites.google.com/site/3demimageprocessing/tomosegmemtv

Amira ver 6.7	Thermo Fisher Scientific	www.thermofisher.com/us/en/home/electron-microscopy/products/software-em-3d-vis/amira-software.html
ChimeraX ver 1.2.1	[56]	www.rbvi.ucsf.edu/chimerax/

Figure 1

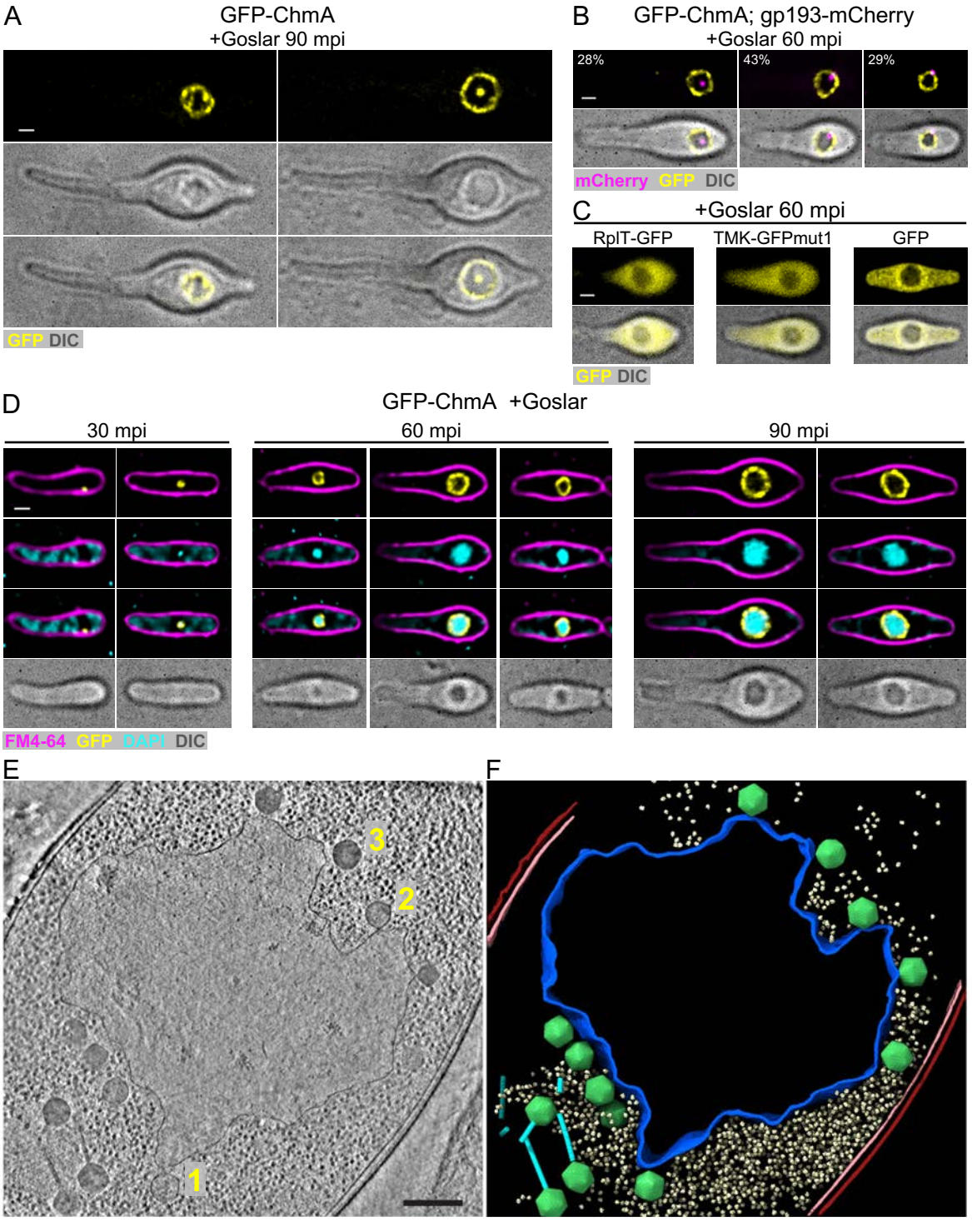
A
GFP-ChmA
+Goslar 90 mpi
GFP DIC
B
GFP-ChmA; gp193-mCherry
+Goslar 60 mpi
28%
43%
29%
mCherry GFP DIC
C
+Goslar 60 mpi
RplT-GFP
TMK-GFPmut1
GFP
GFP DIC
D
GFP-ChmA +Goslar
30 mpi
60 mpi
90 mpi
FM4-64 GFP DAPI DIC
E
3
2
1
F

Figure 2

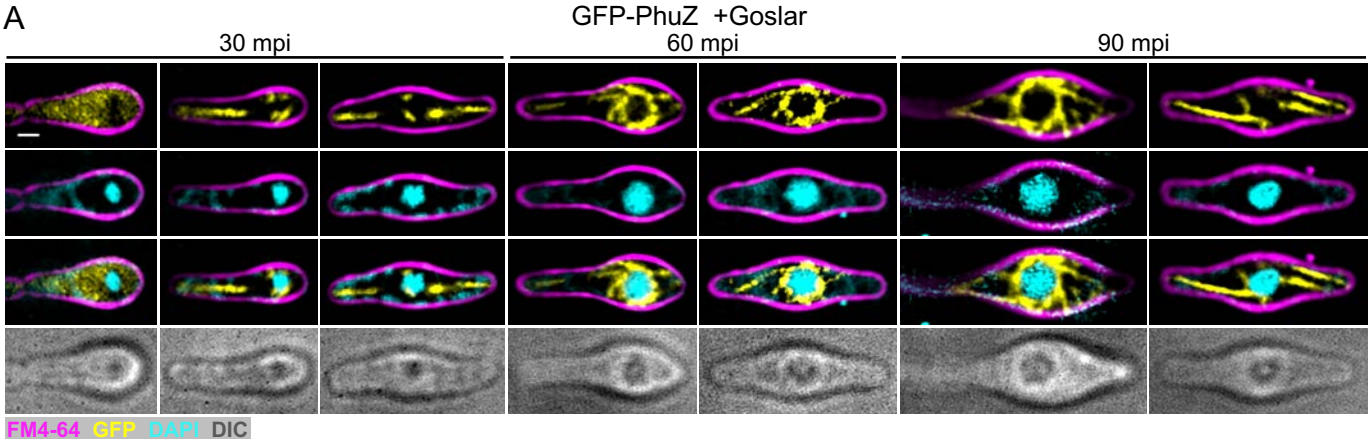
A
GFP-PhuZ +Goslar
30 mpi
60 mpi
90 mpi
FM4-64 GFP DAPI DIC

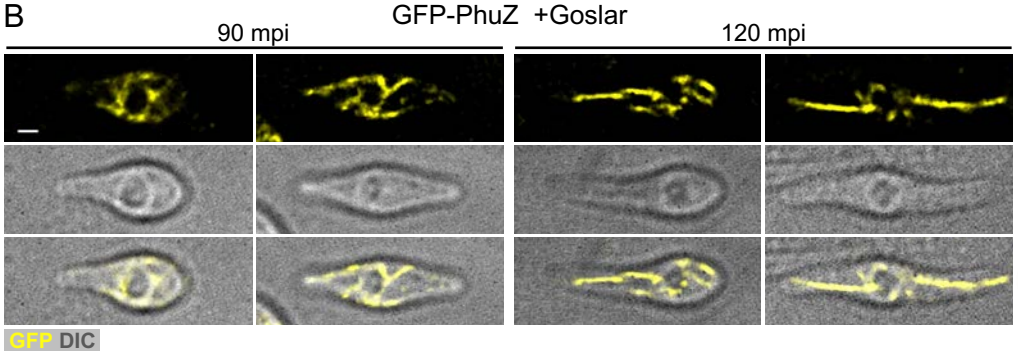
B
GFP-PhuZ +Goslar
90 mpi
120 mpi
GFP DIC

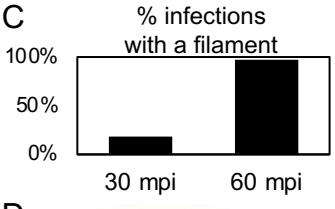
C
% infections
with a filament
100%
50%
0%
30 mpi
60 mpi

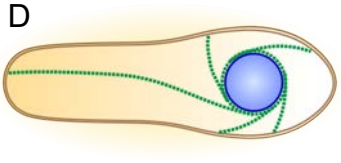
D

Figure 3

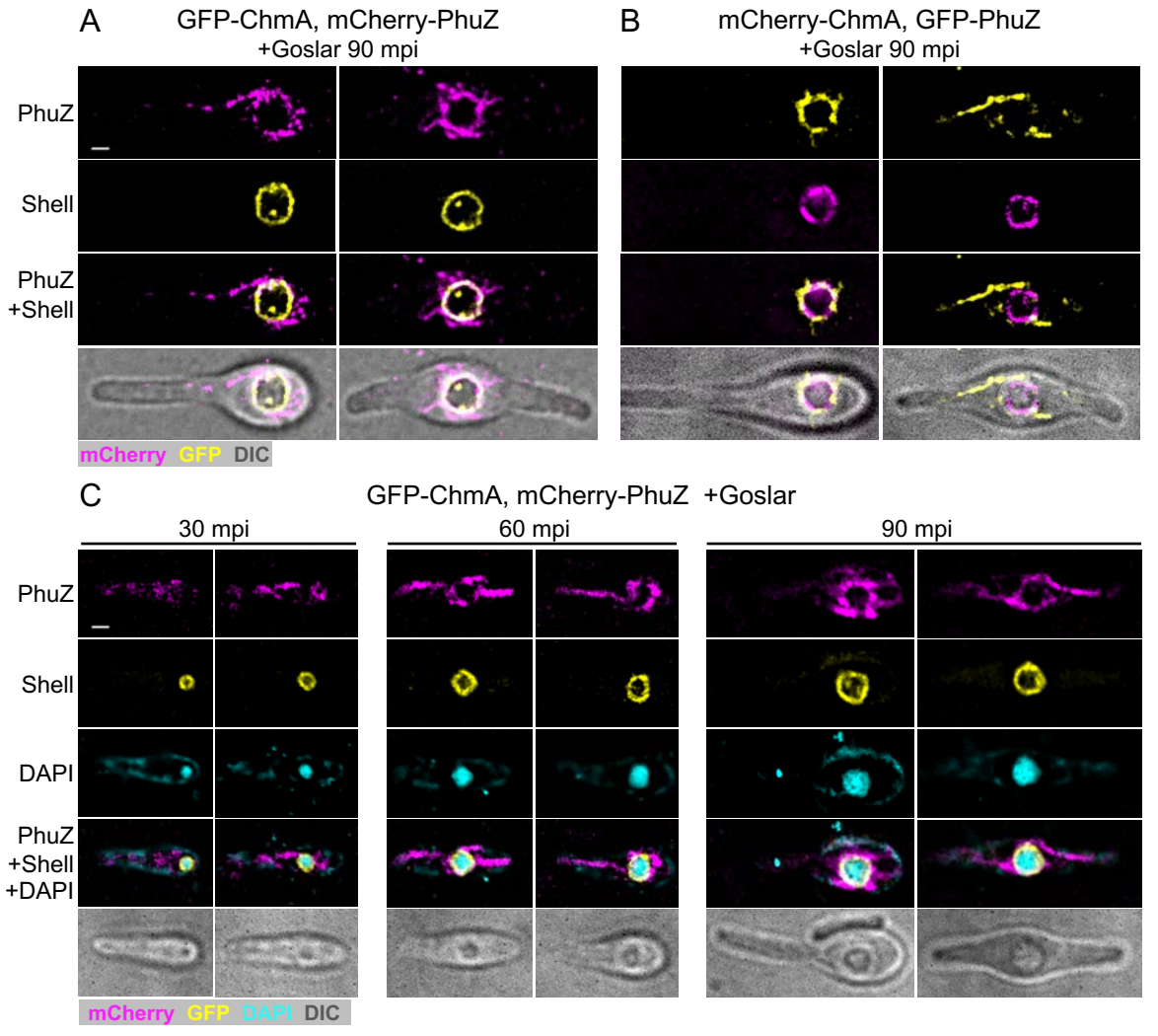
A
GFP-ChmA, mCherry-PhuZ
+Goslar 90 mpi
B
mCherry-ChmA, GFP-PhuZ
+Goslar 90 mpi
PhuZ
Shell
PhuZ
+Shell
mCherry GFP DIC
C
GFP-ChmA, mCherry-PhuZ +Goslar
30 mpi
60 mpi
90 mpi
PhuZ
Shell
DAPI
PhuZ
+Shell
+DAPI
mCherry GFP DAPI DIC

Figure 4

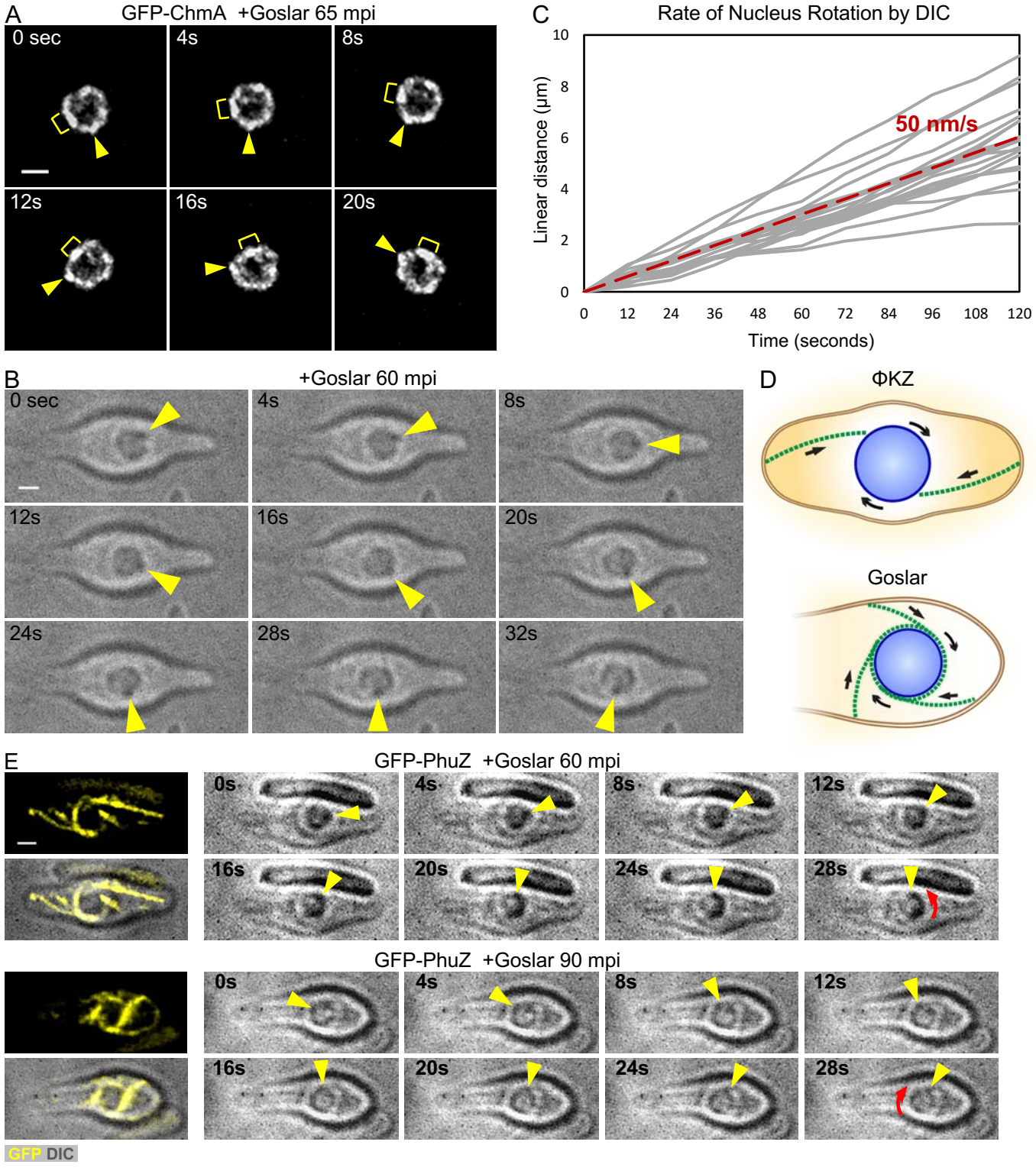
A
GFP-ChmA +Goslar 65 mpi
0 sec
4s
8s
12s
16s
20s
C
Rate of Nucleus Rotation by DIC
Linear distance (µm)
50 nm/s
Time (seconds)
B
+Goslar 60 mpi
0 sec
4s
8s
12s
16s
20s
24s
28s
32s
D
ΦKZ
Goslar
E
GFP-PhuZ +Goslar 60 mpi
0s
4s
8s
12s
16s
20s
24s
28s
GFP-PhuZ +Goslar 90 mpi
0s
4s
8s
12s
16s
20s
24s
28s
GFP DIC

Figure 5

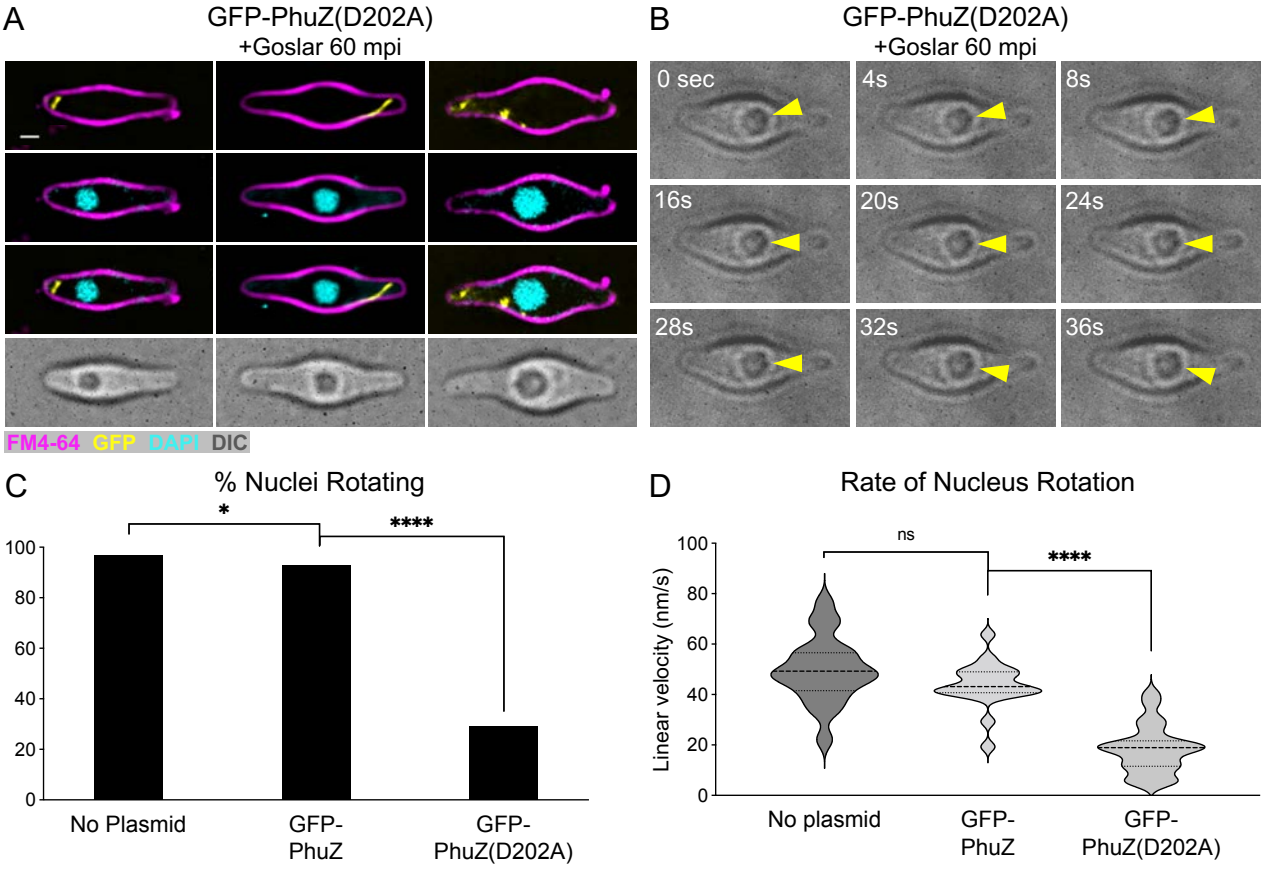
A
GFP-PhuZ(D202A)
+Goslar 60 mpi
FM4-64 GFP DAPI DIC
B
GFP-PhuZ(D202A)
+Goslar 60 mpi
0 sec
4s
8s
16s
20s
24s
28s
32s
36s
C
% Nuclei Rotating
*
****
100
80
60
40
20
0
No Plasmid
GFP-PhuZ
GFP-PhuZ(D202A)
D
Rate of Nucleus Rotation
ns
****
Linear velocity (nm/s)
100
80
60
40
20
0
No plasmid
GFP-PhuZ
GFP-PhuZ(D202A)

Figure 6

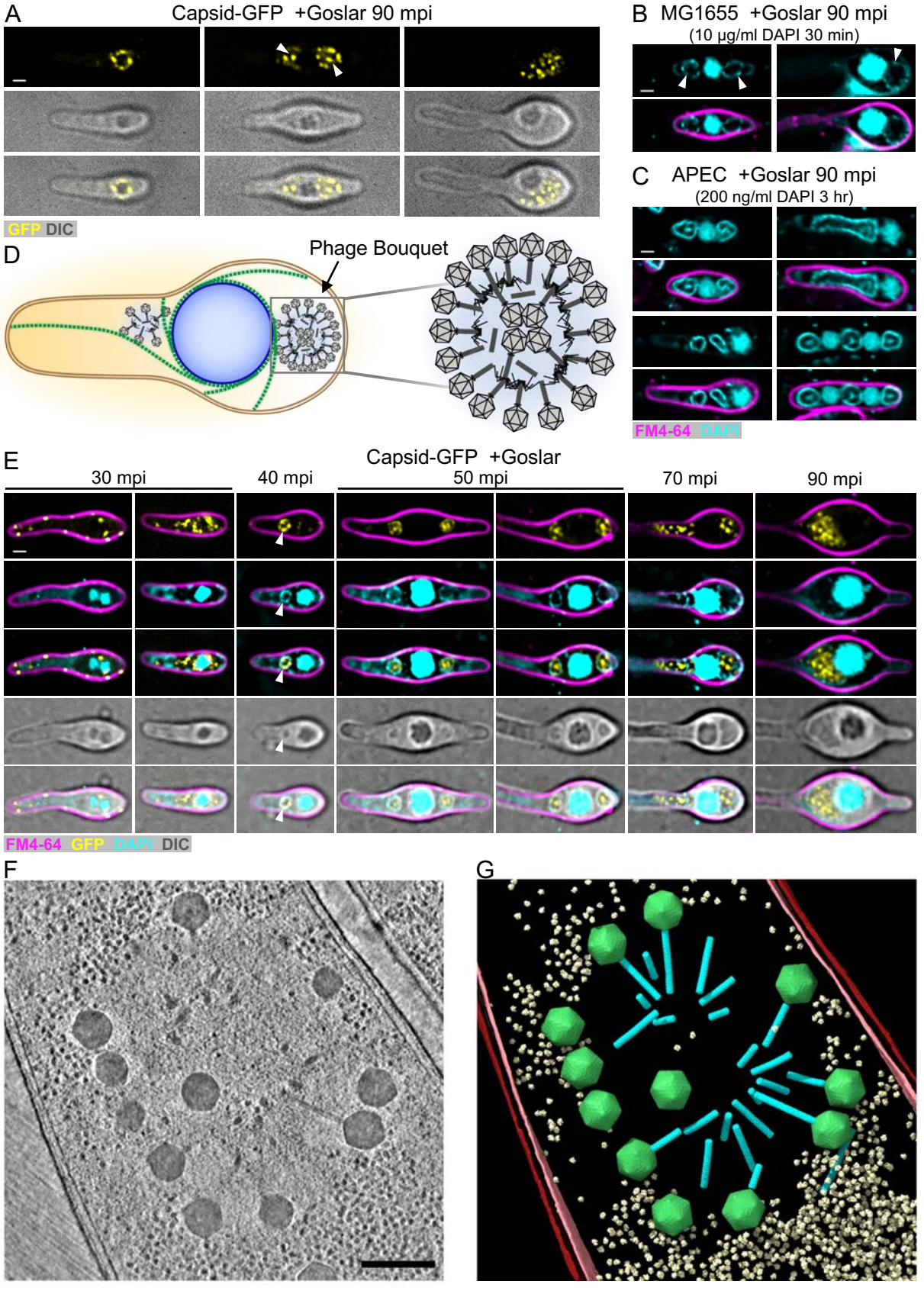
A
Capsid-GFP +Goslar 90 mpi
GFP DIC
B MG1655 +Goslar 90 mpi
(10 μg/ml DAPI 30 min)
C APEC +Goslar 90 mpi
(200 ng/ml DAPI 3 hr)
FM4-64 DAPI
D
Phage Bouquet
E
Capsid-GFP +Goslar
30 mpi
40 mpi
50 mpi
70 mpi
90 mpi
FM4-64 GFP DAPI DIC
F
G

Figure 7

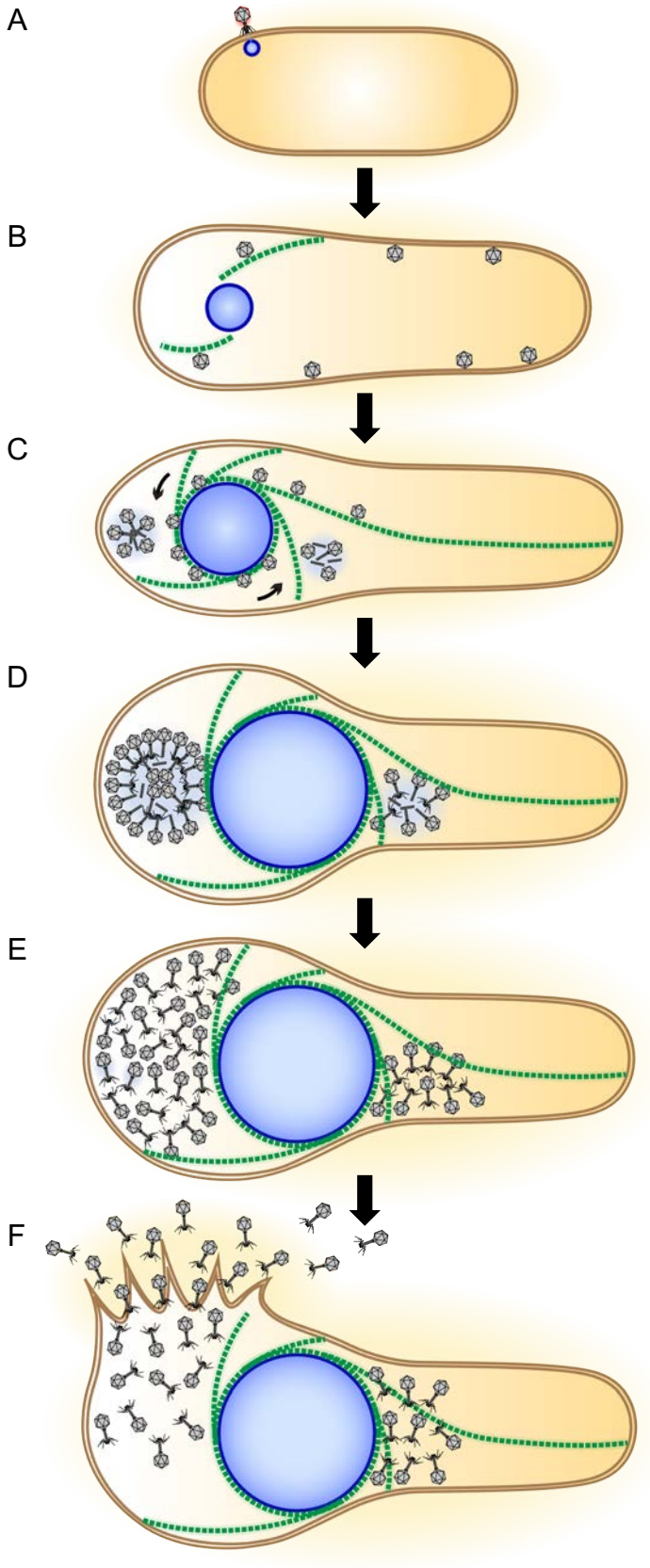

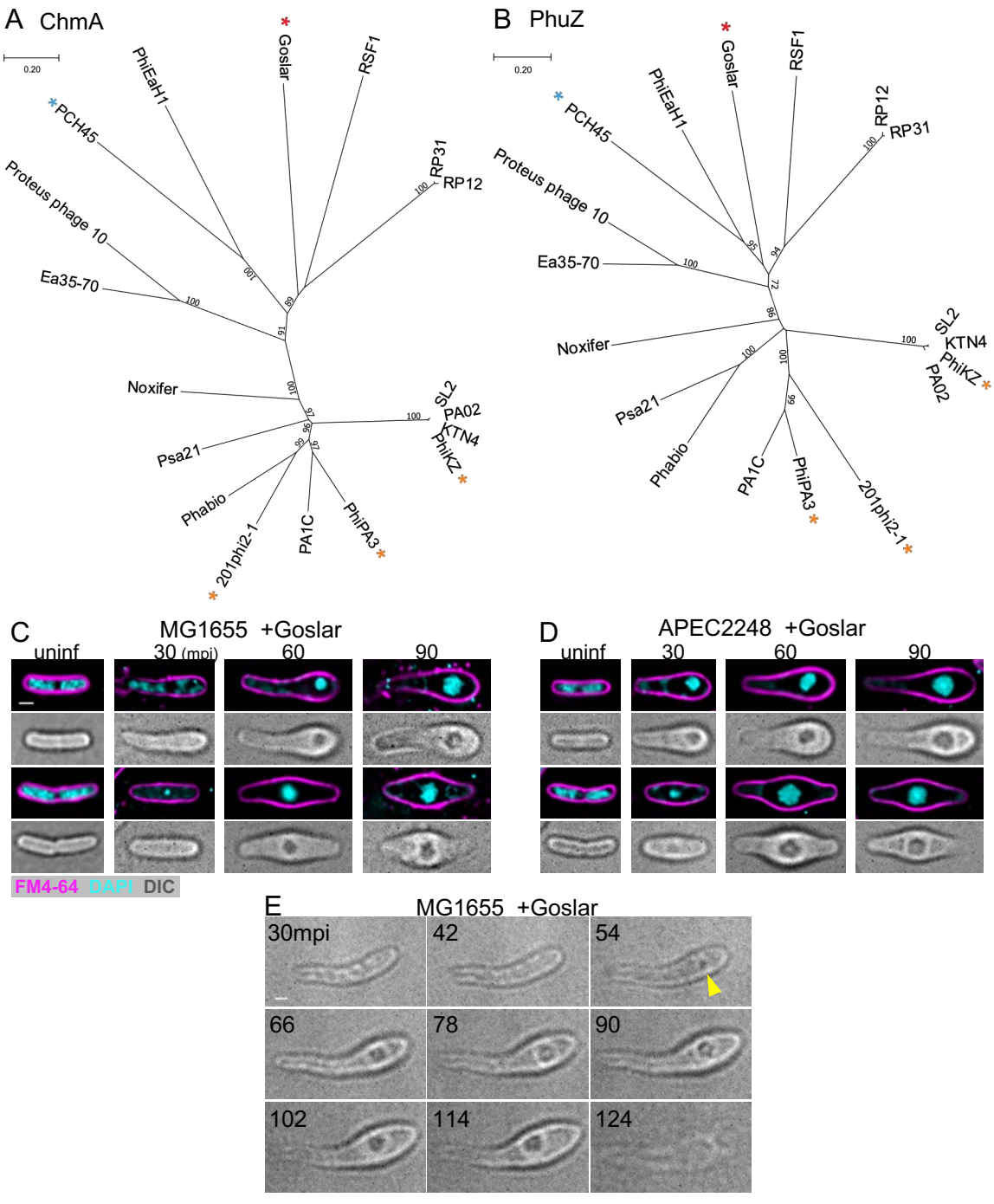

Figure S1. Goslar encodes distant homologs of the major phage nucleus protein chimallin and tubulin-like PhuZ protein and forms a dynamic DNA density during infection. Related to Figures 1 and 2.

(A & B) Unrooted phylogenetic trees of phage nucleus chimallin (ChmA) proteins (A) or phage tubulin PhuZ proteins (B) with bootstrap values (1000 replicates). Red asterisks: Goslar, gold asterisks: characterized nucleus-forming Pseudomonas phages, blue asterisks: nucleus-forming Serratia phage.
(C & D) Two examples of MG1655 cells (C) and APEC cells (D) either uninfected (uninf) or infected by Goslar for 30, 60, or 90 minutes (mpi) then stained with FM4-64 (membrane, magenta) and DAPI (DNA, cyan). A concentrated mass of DNA appears only after addition of phage lysate and this mass can be observed without any fluorescent stains using DIC. All scale bars are 1 μm. Goslar replicates equally well in both strains.
(E) DIC time-lapse every 12 minutes for 94 minutes of MG1655 infected with Goslar for 30 minutes prior to imaging. The DIC density first visible at the yellow arrowhead shows that the nucleoid grows in size and moves around over time as the cell bulges.

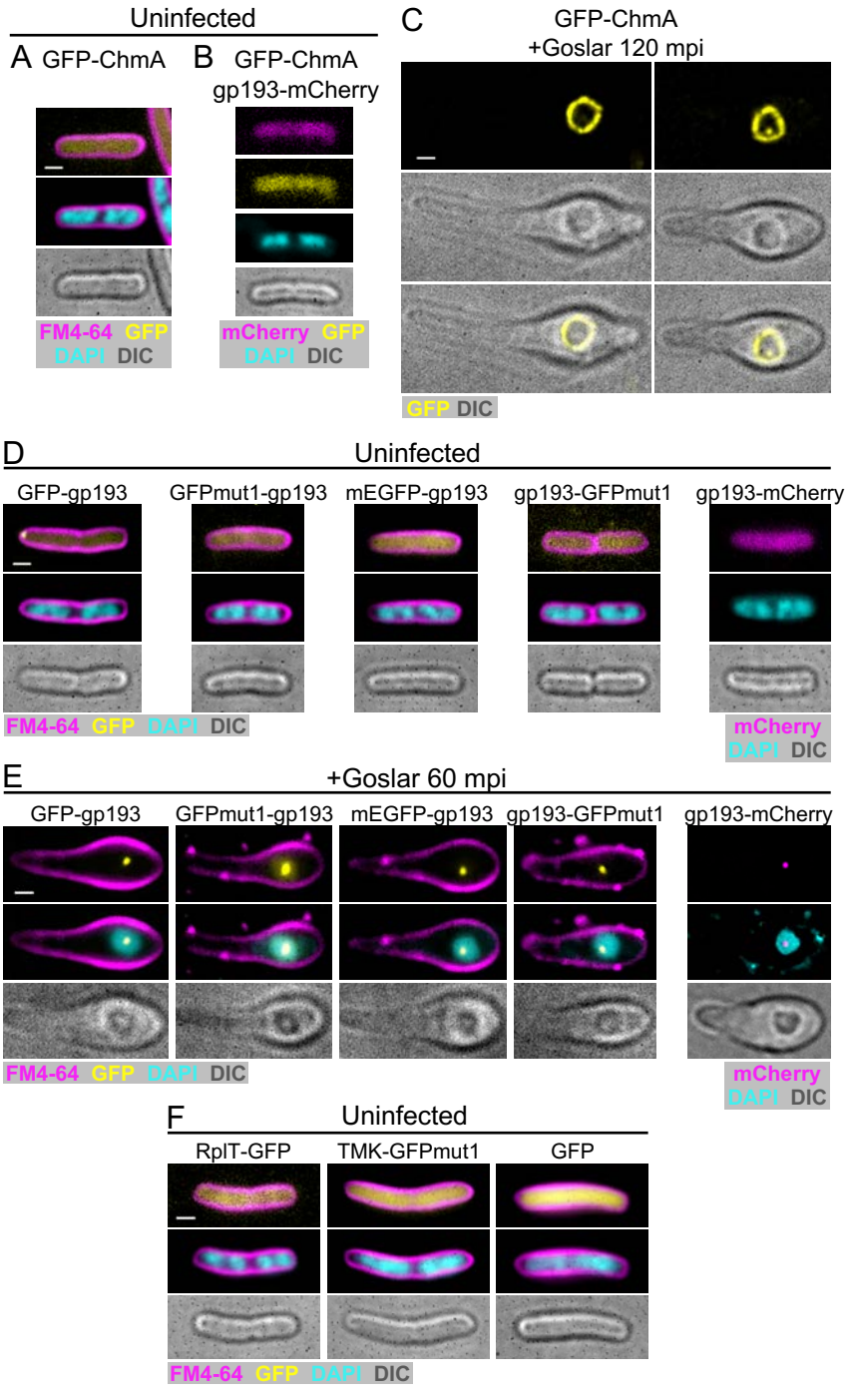

Figure S2. Control experiments show that the fusion proteins do not form specific structures in uninfected cells and that the choice of fusion does not alter the results. Related to Figure 1.

(A) *E. coli* (MG1655) expressing GFP-ChmA induced with 0.2 mM IPTG for 1.5 hours (uninfected). All scale bars are 1 μm.

(B) E. coli co-expressing GFP-ChmA with gp193-mCherry and induced at 0.2 mM IPTG for 1.5 hours then stained with DAPI (uninfected).
(C) E. coli expressing GFP-ChmA induced with 0.2 mM IPTG and infected by Goslar for 120 minutes.
(D) E. coli expressing each gp193 fusion indicated and induced at 0.2 mM IPTG for 1.5 hours then stained with FM4-64 and DAPI, or just DAPI for gp193-mCherry (uninfected). Fusions to different fluorescent proteins (mCherry, mEGFP, GFPmut1) are generally uniformly distributed throughout the cell, only GFP-gp193 forms a polar punctum.
(E) E. coli expressing the listed gp193 fusion protein at 0.2 mM IPTG, infected by Goslar for 60 minutes then stained with FM4-64 and DAPI. Fusing different fluorescent proteins (mCherry, GFP, mEGFP, GFPmut1) to gp193 at either the N- or C-terminus produces the same results.
(F) E. coli expressing 50S ribosomal protein L20 (RplT-GFP), thymidylate kinase (TMK-GFP), or GFP alone, induced at 0.2 mM IPTG for 1.5 hours then stained with FM4-64 and DAPI. These fusions are generally uniformly distributed throughout the cell.

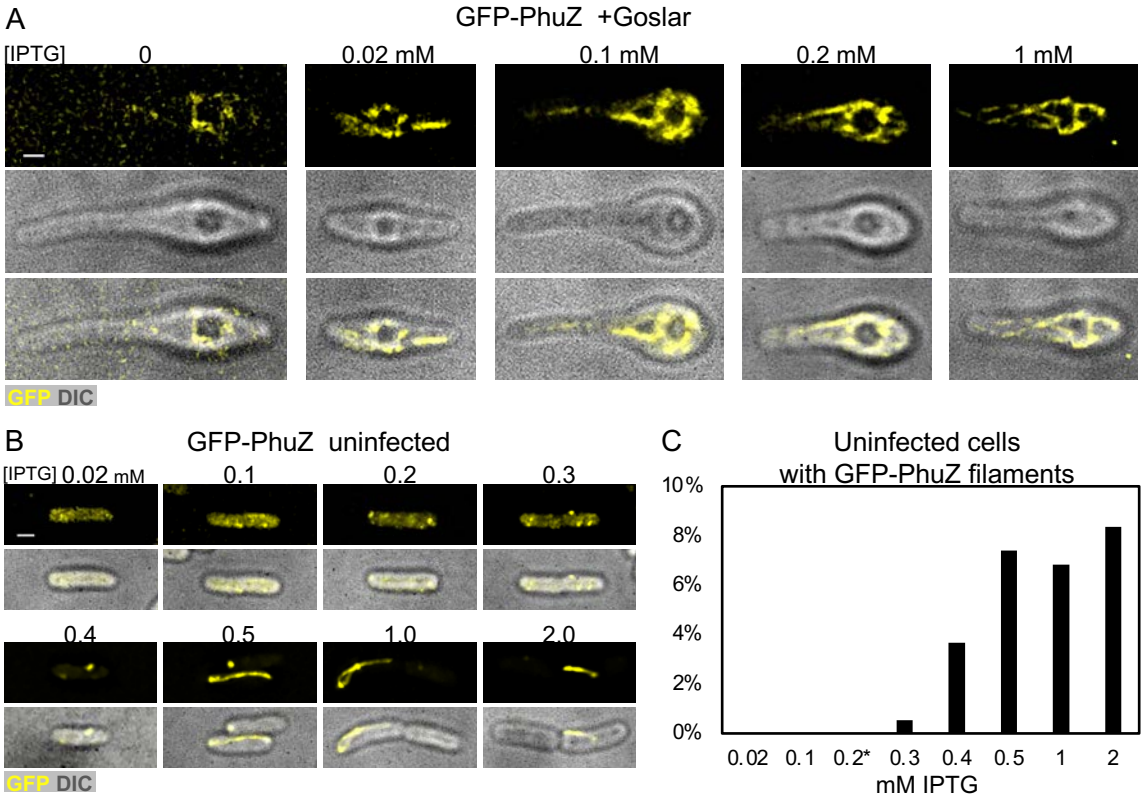

Figure S3. Assembly of GFP-PhuZ in uninfected and infected cells. Related to Figure 2.

(A) GFP-PhuZ accumulates around the phage nucleus even when expressed at very low levels. All levels of induction by IPTG show a similar vortex-like phenotype. All scale bars are 1 μm.

(B) Uninfected *E. coli* (MG1655) expressing GFP-PhuZ (yellow) does not form filaments over 0.3 μm in length until 0.3 mM IPTG.

(C) Percent of uninfected cells with a PhuZ filament over 0.3 μm at IPTG concentrations from 0.02 - 2.0 mM (0.02, n=78; others, n > 100).

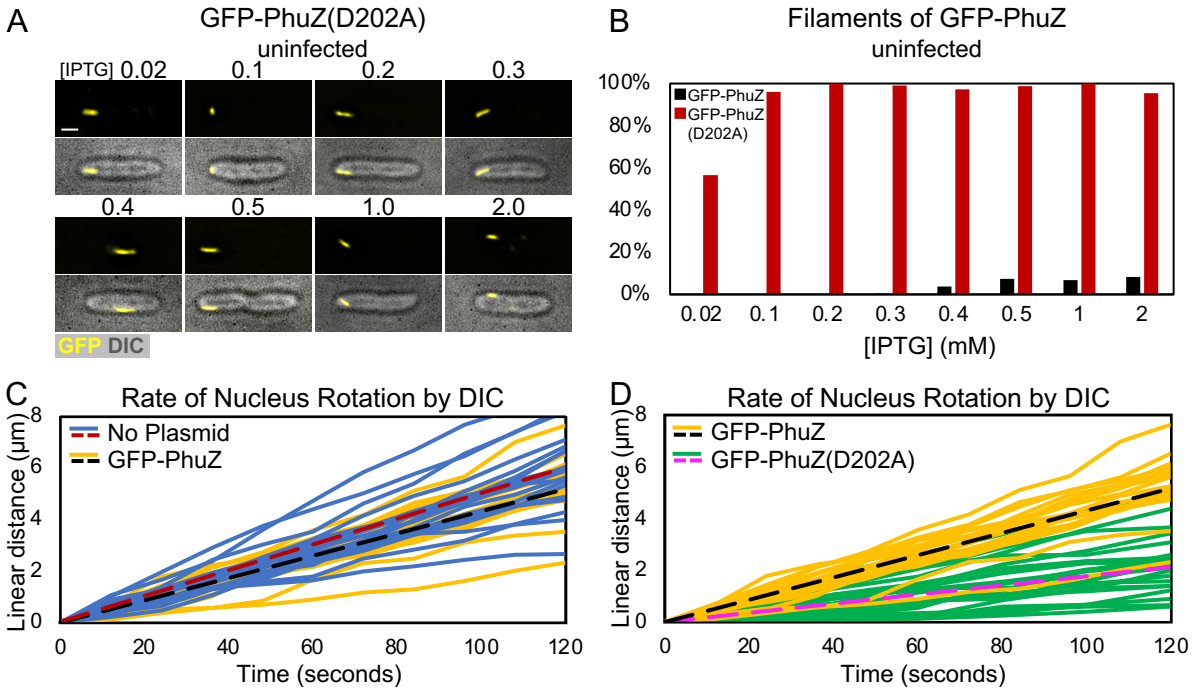

Figure S4. Expression of a catalytically defective PhuZ, GFP-PhuZ(D202A), alters PhuZ assembly properties and phage nucleus rotation. Related to Figure 6.

(A) Uninfected *E. coli* (MG1655) expressing GFP-PhuZ(D202A) induced with 0.02-2.0 mM IPTG and grown on 50 μg/ml ampicillin for 90 minutes. Scale bar 1 μm.

(B) Percentage of cells expressing either GFP-PhuZ(D202A) (red) or GFP-PhuZ (black) that contained filaments over 0.3 μm at each IPTG concentration (0.2, n = 99; 0.5, n = 85; others, n > 100).

(C) Linear velocity of nuclear rotation of 20 measured nuclei for *E. coli* (blue solid lines; average, red dotted line) compared to those in *E. coli* expressing GFP-PhuZ (yellow solid lines; average, black dotted line), 60 minutes after the addition of Goslar.

(D) Linear velocity of nuclear rotation of 20 measured nuclei in *E. coli* expressing GFP-PhuZ (yellow solid lines; average, black dotted line) compared to the 23 nuclei in *E. coli* expressing GFP-PhuZ(D202A) (green solid lines; average, magenta dotted line), 60 minutes after the addition of Goslar.

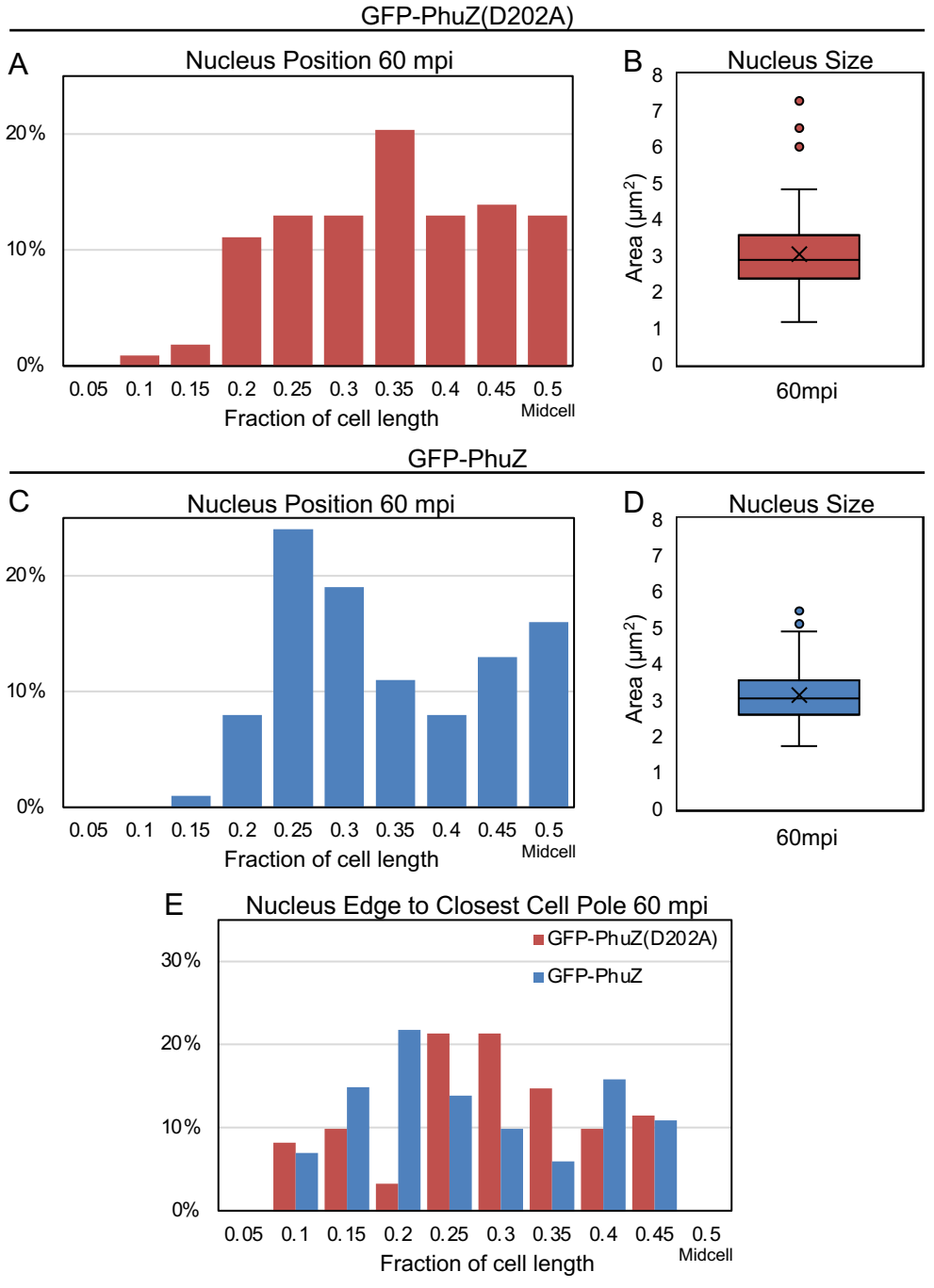

Figure S5. PhuZ(D202A) expression does not affect Goslar nucleus positioning or size. Related to Figure 6.

(A) Distribution of 60 mpi phage nuclei (DIC) along the lateral length of *E. coli* (MG1655) expressing GFP-PhuZ(D202A) induced with 0.2 mM IPTG. For each time point, there is no significantly greater chance of finding a phage nucleus in one certain bin than in the neighboring bins (n=108).

(B) 2D area of the DAPI-stained 60 mpi phage nucleus in the presence of GFP-PhuZ(D202A) (n=108).
(C) Distribution of 60 mpi DIC phage nuclei along the lateral length of *E. coli* expressing GFP-PhuZ induced with 0.2 mM IPTG. For each time point, there is no significantly greater chance of finding a phage nucleus in one certain bin than in the neighboring bins (n=100).
(D) 2D area of the DAPI-stained 60 mpi phage nucleus in the presence of GFP-PhuZ (n=111).
(E) Distribution of distances between the edge of the phage nucleus to the closest cell pole, normalized to cell length. Either GFP-PhuZ(D202A) or GFP-PhuZ was infected for 60 minutes and stained with FM4-64 and DAPI. DIC was used for measurement (n=88).

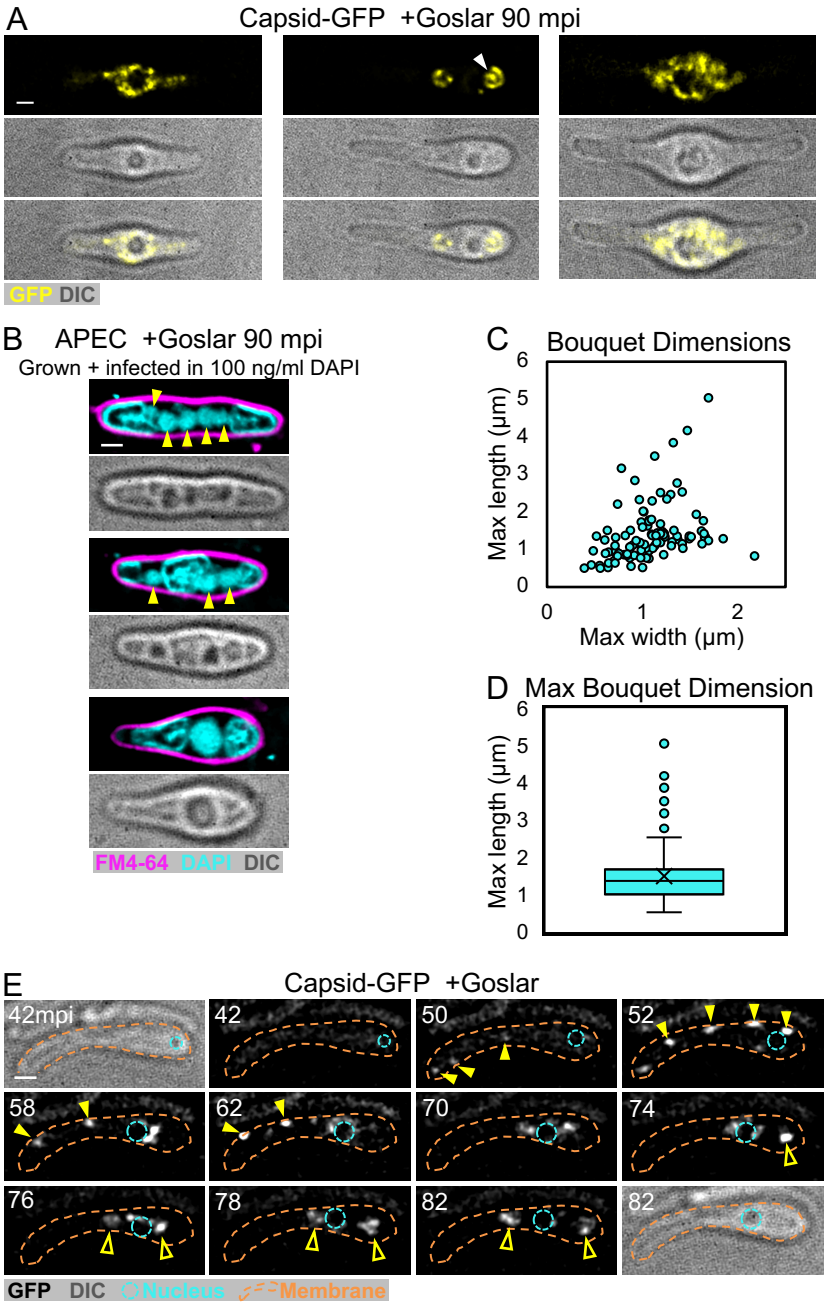

Figure S6. Capsid-GFP localization and bouquet formation during Goslar infections. Related to Figure 7.

(A) More examples of capsid-GFP localization as in Figure 7A. *E. coli* (MG1655) expressing the putative capsid protein (gp41) fused to GFP (yellow) induced with 0.2 mM IPTG and infected with Goslar for 90 minutes. Capsids localized around the phage nucleus (left panels), in adjacent bouquets (middle panels), or filling more of the cytoplasm (right panels). All scale bars are 1 µm.

(B) Additional examples of multiple nuclei and bouquets (top four panels) and a single nucleus (bottom two panels) imaged by DAPI and FM4-64 after 90 mpi in APEC (yellow arrowheads indicate nuclei). Top 2 panels show 5 nuclei observed in one cell, middle 2 panels show 3 nuclei with a large central bouquet, bottom panels show a single nucleus with the most common bouquet phenotype.
(C) DAPI-stained bouquets at 90 mpi in APEC were measured along the maximum x and y dimensions. Each point represents one bouquet (n=105).
(D) Box and whisker plot of maximum bouquet dimension for each bouquet in (C). Quartiles are calculated with an excluded median and a mean of 1.5 μm (n=105).
(E) Time-lapse of capsid-GFP (white) at various intervals over 40 minutes starting at 42 mpi in MG1655. Capsids migrate from the cell periphery or cytoplasm (yellow solid arrowheads) to the phage nucleus exterior and then to adjacent phage bouquets (yellow open arrowheads) (cyan dashed line, nucleus; orange dashed line, cell membrane).

Table S1. *E. coli* strains used in this study. Related to STAR Methods.				
Strain	**Plasmid**	**Expression Protein** [b]	**Function**	**Host**
EB293	pEB183[a]	GFP-gp201	PhuZ - cytoskeleton	MG1655
EB285	pEB181[a]	GFP-gp189	Phage nucleus shell (chimallin)	MG1655
EB315	pEB203[a]	GFP-gp193	gp193 - unknown function	MG1655
EB320	pEB205[a]	GFPmut1-gp193	gp193	MG1655
EB316	pEB204[a]	mEGFP-gp193	gp193	MG1655
EB317	pEB206[a]	gp193-GFPmut1	gp193	MG1655
EB318	pEB208[a]	gp193-mCherry	gp193	MG1655
EB333	pEB201[a]	GFP-gp189; gp193-mCherry	ChmA co-expressed with gp193	MG1655
EB308	pEB191[a]	RplT-GFP	L20 ribosomal subunit (MG1655)	MG1655
EB309	pEB192[a]	TMK-GFPmut1	Thymidylate kinase	MG1655
EB301	pEB173	GFP	Free fluorophore control	MG1655
EB295	pEB185[a]	GFP-gp189; mCherry-gp201	ChmA co-expressed with PhuZ	MG1655
EB314	pEB202[a]	mCherry-gp189; GFP-gp201	ChmA co-expressed with PhuZ	MG1655
EB312	pEB196[a]	GFP-PhuZ(D202A)	Catalytically dead PhuZ	MG1655
EB297	pEB190[a]	gp41-GFP	Capsid	MG1655

[a] Synthesized and cloned by Genscript.

[b] "GFP" – Addgene pTD103luxI_GFP [61] with mutations S2A, T65G, D190/197H.